Wound Healing Capacity as a Biomarker of Aging Resilience: Behavioral and Transcriptomic Characterization of High and Low Responder Phenotypes

Ankita Sharma

A thesis

submitted in partial fulfillment of the

requirements for the degree of

Master of Science

University of Washington

2026

Committee:

Warren Ladiges

Brian Iritani

Christina Pettan-Brewer

Program Authorized to Offer Degree:

Comparative Medicine

University of Washington

Abstract

Wound Healing Capacity as a Biomarker of Aging Resilience: Behavioral and Transcriptomic Characterization of High and Low Responder Phenotypes

Ankita Sharma
Chair of the Supervisory Committee:
Warren Ladiges
Department of Comparative Medicine

Age-related decline in physiological resilience manifests across cognitive, physical, and metabolic domains, yet validated early biomarkers capable of predicting individual aging trajectories before functional decline occurs remain lacking. Wound healing capacity represents a promising candidate biomarker because successful tissue repair requires coordinated function of the same immune, vascular, metabolic, and cellular stress response systems whose deterioration underlies broader aging vulnerability. To test this, aged C57BL/6J mice (n=80, 40 male, 40 female, 18 months) underwent a standardized 2mm ear punch biopsy and were stratified by median wound closure at Day 16 into high responders (n=28) and low responders (n=28). Ten mice exhibiting net wound enlargement were excluded from primary analyses as a biologically distinct subgroup. Cognitive and physical function were assessed at 24 to 25 months across four behavioral assays, followed by tissue collection for RNA sequencing of hippocampus and liver and immunohistochemical analysis of brain tissue. In the filtered cohort (n=56), high healers significantly outperformed low healers on rotarod performance ($t = 2.309$, $df = 50.13$, $p = 0.025$). Sex-stratified analyses revealed wound healing capacity was significantly correlated with rotarod performance in males ($rs = 0.575$, $p = 0.003$), with high-healing males demonstrating substantially longer latency to fall than low-healing males ($t = 2.597$, $df = 21.42$, $p = 0.017$). Spearman's correlation analysis identified a significant negative relationship between wound healing capacity and hippocampal IBA1 expression in the full filtered cohort ($rs = -0.302$, $p = 0.024$), driven primarily by female mice ($rs = -0.404$, $p = 0.024$), suggesting that poor wound healing co-occurs with greater hippocampal microglial burden in females. Hippocampal RNA sequencing identified the Hallmark Interferon Alpha Response as significantly enriched in high responders by gene set enrichment analysis (NES = 1.71, FDR = 0.016), with stress axis genes Fkbp5 and Klf9 trending downward in the resilient phenotype. Liver transcriptomics identified 14 differentially expressed genes, with high responders showing upregulation of stress response and detoxification genes including Gadd45g and Gstm3 and strong downregulation of the circadian clock repressor Ciart. Low responder livers were significantly enriched for hallmarks of systemic inflammaging including IL6/JAK/STAT3 signaling, complement activation, interferon gamma response, and markers of elevated cellular stress and hepatocyte turnover. These findings demonstrate that wound healing capacity stratifies aged mice into biologically distinct molecular phenotypes, supporting its utility as a tractable, minimally invasive biomarker for early identification of vulnerable aging phenotypes. Identified transcriptomic signatures provide candidate targets for future resilience-promoting interventions.

Keywords: aging resilience, wound healing, biomarker, inflammaging, RNA sequencing, gene set enrichment analysis, immunohistochemistry, C57BL/6J, hippocampus, liver, circadian clock, gerotherapeutics

Acknowledgements

I am extremely thankful to each of my committee members, Dr. Brian Iritani and Dr. Christina Pettan-Brewer, for their commitment to my success, valuable advice, and constant support throughout this process. I want to give a special thanks to my mentor and committee supervisor, Dr. Warren Ladiges, for his unwavering support throughout my graduate education, his continuous guidance, and his dedication to encouraging my passion for this work.I want to offer my sincere thanks to everyone within the Ladiges Lab, each of whom contributed to this project in ways both large and small. Jackson Wezeman provided invaluable help with wound healing ear punches, necropsies, box maze, and offered expertise and support at every turn. Addison Keeley assisted with necropsies and brought deep IHC expertise to this project, and I am especially grateful for the extraordinary number of slides she cut on my behalf. John Morton provided essential guidance on lab guidelines and resources. Ada Lu helped with mouse handling and Y-maze procedures, and stepped up to keep things moving during moments when I needed it most. Sonali Bhana offered critical IHC support at a pivotal time in data collection. Jerry Liao generously shared his bioinformatics expertise and encouragement throughout the computational work. Sy Fatemie-Nainie made the day-to-day of graduate school considerably better simply by being a great bay-mate. Though they had graduated before this project was complete, Manuela Rosenfeld and Jordan Mazzola left behind a framework, a standard, and a spirit of mentorship that shaped this work in lasting ways. Finally, Dr. Ruby Sue Mangalindan deserves special recognition for teaching me everything I know about mouse handling and setting me up to succeed from the very beginning.

This work was supported by the National Institutes of Health, National Institute on Aging grant R01-AG057381 (PI: Warren Ladiges).

Dedication

I would like to dedicate this work to my family and friends, including but not limited to my mom, dad, and brother, all of whom have supported me every step of the way. I would also like to recognize the laboratory mice who gave their lives in service of science. Without them, none of this would have been possible.

Table of Contents

Introduction

The global population aged 65 and older will double by 2050, creating an unprecedented healthcare burden (United Nations, 2019; Beard et al., 2016). Current systems remain unprepared to manage this demographic shift, which necessitates interventions promoting healthy aging rather than merely extending lifespan. A fundamental challenge complicates this goal: chronological age provides an inadequate measure of biological aging. Two individuals of identical chronological age may exhibit vastly different functional capacities, revealing that chronological and biological age are not equivalent (Ferrucci et al., 2020). This heterogeneity in aging trajectories highlights a critical gap in our ability to predict individual aging outcomes before functional decline manifests.

Contemporary approaches to aging healthcare remain predominantly reactive. Existing biomarkers measure frailty, cognitive impairment, or metabolic dysfunction after these conditions have already developed, followed by attempts to manage consequences rather than prevent decline (López-Otín et al., 2013). A fundamental barrier to progress is the lack of validated, early-detectable biomarkers of resilience that can predict functional outcomes before significant decline has occurred (Kennedy et al., 2014). What is needed instead is a proactive, predictive approach requiring validated biomarkers that assess physiological reserve capacity and predict future trajectories before irreversible functional decline occurs, when interventions retain maximum effectiveness.

Resilience, defined as the ability to maintain or recover function despite physical stressors, provides a framework for understanding why individuals age differently (Whitson et al., 2016). Whether facing infection, injury, or metabolic stress, resilient individuals preserve function and recover efficiently. In contrast, vulnerable individuals show protracted impairment. This capacity reflects coordinated function across multiple interconnected physiological systems, including immune regulation, vascular health, metabolic homeostasis, and cellular stress responses, rather than any single organ or pathway (López-Otín et al., 2023). Understanding the mechanisms underlying this heterogeneity and identifying early biomarkers of resilience capacity represents a critical frontier in aging research with profound implications for promoting healthy longevity.

Individual variation in the trajectory of age-related changes suggests that early indicators of physiological resilience may exist and could predict later-life functional outcomes. Recent progress in aging biology has identified hallmarks of aging including genomic instability, telomere attrition, loss of proteostasis, disabled macroautophagy, deregulated nutrient-sensing, mitochondrial dysfunction, cellular senescence, stem cell exhaustion, altered intercellular communication, dysbiosis, and chronic inflammation (López-Otín et al., 2023). These hallmarks operate in concert, such that decline in one system often exacerbates dysfunction in others. Identifying biomarkers capturing these interconnected processes would enable stratification of individuals based on biological rather than chronological age, facilitating targeted interventions for those at greatest risk of poor aging outcomes.

Age-related cognitive decline (ARCD) represents a process of particular concern due to its high prevalence and profound impact on quality of life. Cognitive function declines progressively with age across multiple domains, with the global prevalence of mild cognitive impairment ranging from approximately 5% to 41% in community-dwelling adults aged 60 and older, with a median of approximately 19% (Pais et al., 2020; Harada et al., 2013). ARCD is characterized by

memory loss, neuronal dysfunction, chronic inflammation, and increased cellular senescence in brain regions such as the hippocampus and cerebellum (Murman, 2015; Bettio et al., 2017). Beyond its direct effects on cognitive function, ARCD serves as a significant risk factor for more severe neurodegenerative diseases including dementia and Alzheimer's disease (Petersen et al., 2018). Despite its high prevalence and profound impact on daily life, no treatments are currently available to prevent or reverse ARCD, presenting a serious knowledge gap and clinical shortcoming.

Wound healing capacity represents a promising candidate biomarker of physiological resilience. The wound healing process is fundamentally integrative, requiring coordinated function of multiple physiological systems central to aging resilience (Broughton et al., 2006). Successful repair demands robust immune function for debris clearance and infection prevention, adequate vascular function for nutrient and oxygen delivery to wound sites, effective tissue remodeling to rebuild damaged structures, and sufficient metabolic regulation to fuel this energetically demanding process (Broughton et al., 2006; Guo & DiPietro, 2010). Appropriate stress response pathways coordinate the entire cascade. These systems enabling wound healing are precisely those whose age-related decline contributes to broader resilience deficits and susceptibility to multiple age-related diseases.

In humans, wound healing capacity serves as a clinically relevant indicator of physiological reserve that becomes increasingly important with advancing age (Gould et al., 2015). Chronic wounds affect approximately 6.5 million Americans annually, with healing complications disproportionately affecting older adults and resulting in substantial morbidity and healthcare costs (Sen et al., 2009). Age-related impairments in wound healing reflect systemic changes in immune regulation, vascular health, collagen synthesis, and growth factor signaling that parallel the pathophysiological hallmarks of aging at the tissue level (Sgonc & Gruber, 2013; Khalid et al., 2022). These biological processes contribute not only to wound repair but also to cognitive function, cardiovascular health, and metabolic regulation. Individual variation in wound healing capacity among older adults suggests this measure captures fundamental differences in biological aging that extend beyond local tissue repair mechanisms (Ashcroft et al., 1995). Patients demonstrating superior wound healing often exhibit better overall health outcomes across multiple domains, supporting the hypothesis that wound repair capacity reflects systemic resilience (Guo & DiPietro, 2010).

Assessment of wound healing capacity is possible relatively early in aging through minimally invasive procedures, creating potential for identifying at-risk individuals when preventive interventions may retain effectiveness. Unlike biomarkers requiring specialized imaging or extensive laboratory analyses, wound healing assessment is straightforward, quantifiable, and amenable to standardization. These characteristics enhance its potential utility as a screening tool in preclinical aging research, with molecular signatures identified through this approach providing the foundation for future translatable biomarker development.

Preliminary work from our laboratory has provided proof-of-concept evidence that wound healing capacity predicts broader resilience outcomes. Jiang and colleagues (2020) assessed wound healing in female C57BL/6J mice at 20 months of age using a standardized 2-millimeter ear punch biopsy. Based on wound closure at week 2, when healing differences were most pronounced, mice were categorized as fast or slow healers. Functional testing occurred 3 months later at 23 months of age, establishing temporal separation between biomarker assessment and

outcome measures. This temporal design tests whether wound healing predicts future function rather than merely correlating with concurrent performance. Fast healers significantly outperformed slow healers across multiple functional domains. Superior spatial learning was demonstrated in the box maze escape task, along with greater forelimb grip strength and enhanced running endurance on voluntary wheel running tests (Jiang et al., 2020).

These differences spanned both cognitive and physical performance domains, indicating that wound healing capacity reflects systemic resilience rather than domain-specific function.

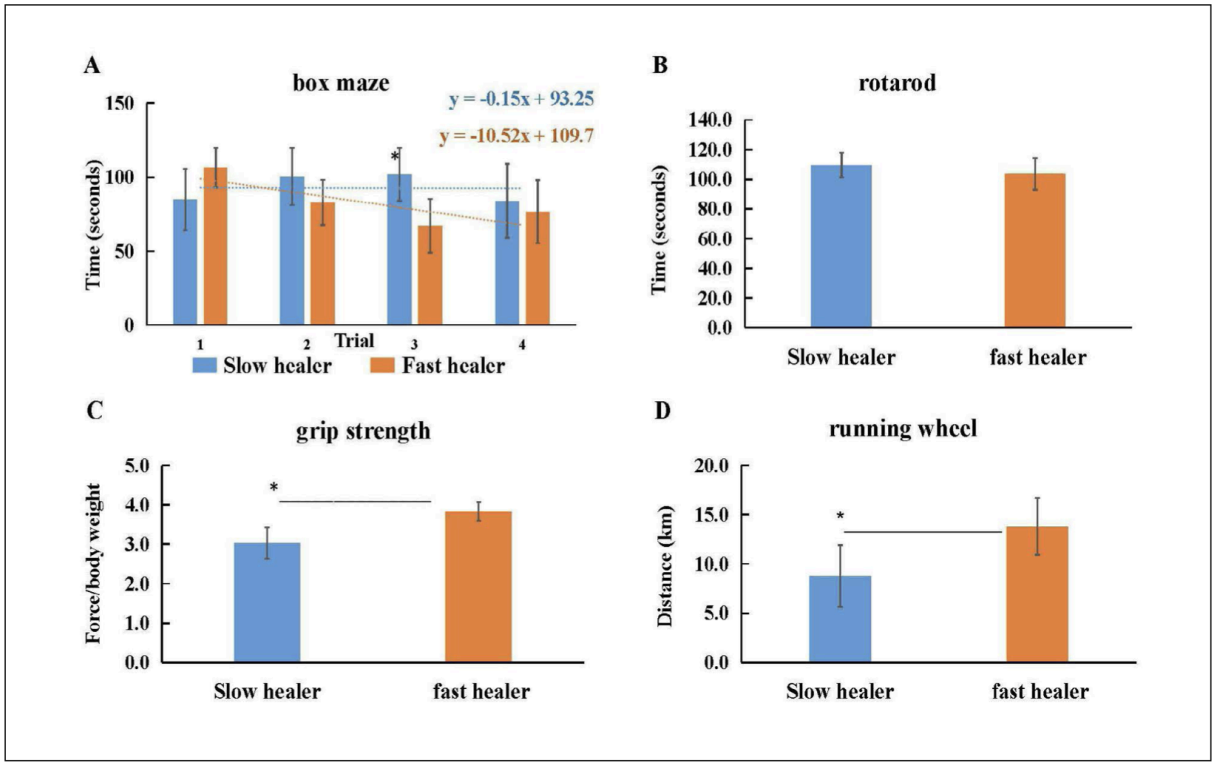

Figure 1. Preliminary data from Jiang et al. (2020) showing wound healing capacity at 20 months predicts functional outcomes at 23 months in female C57BL/6J mice. A. Escape latency across four box maze trials with linear regression slopes shown. B. Rotarod latency to fall. C. Forelimb grip strength normalized to body weight. D. Voluntary running wheel distance. *p < 0.05 by two-sample t-test. Data presented as mean ± SEM. Adapted from Jiang et al., Aging Pathobiology and Therapeutics, 2020.

While this preliminary study established feasibility and initial validation of the approach, critical questions remain. Comprehensive characterization of specific resilience domains affected by wound healing capacity is needed, as the relationship between wound healing and aging outcomes has not been examined across both sexes or multiple functional domains simultaneously. The molecular mechanisms distinguishing resilient from vulnerable phenotypes are uncharacterized. Which biological pathways drive observed differences in aging trajectories, including inflammatory regulation, mitochondrial function, cellular stress responses, or synaptic plasticity, remains unknown. Elucidating these mechanisms is essential for both biological understanding and identification of potential therapeutic targets.

The C57BL/6J mouse model provides a translationally relevant and experimentally tractable system for investigating individual variation in aging resilience. Mouse models offer several advantages, including relatively short lifespans enabling longitudinal studies within practical timeframes, genetic homogeneity reducing confounding variation, and controlled environmental conditions enhancing experimental rigor (Yanai & Endo, 2021). Cognitive impairment in C57BL/6J mice increases progressively with age. At 20 months, mice display intermediate cognitive deficits compared to younger cohorts, while 28-month-old mice exhibit the most severe impairments (Daneshjoo et al., 2022). Despite genetic homogeneity and identical environmental conditions, substantial individual variation exists in aging trajectories within this strain, enabling investigation of factors predicting divergent aging outcomes (Daneshjoo et al., 2022).

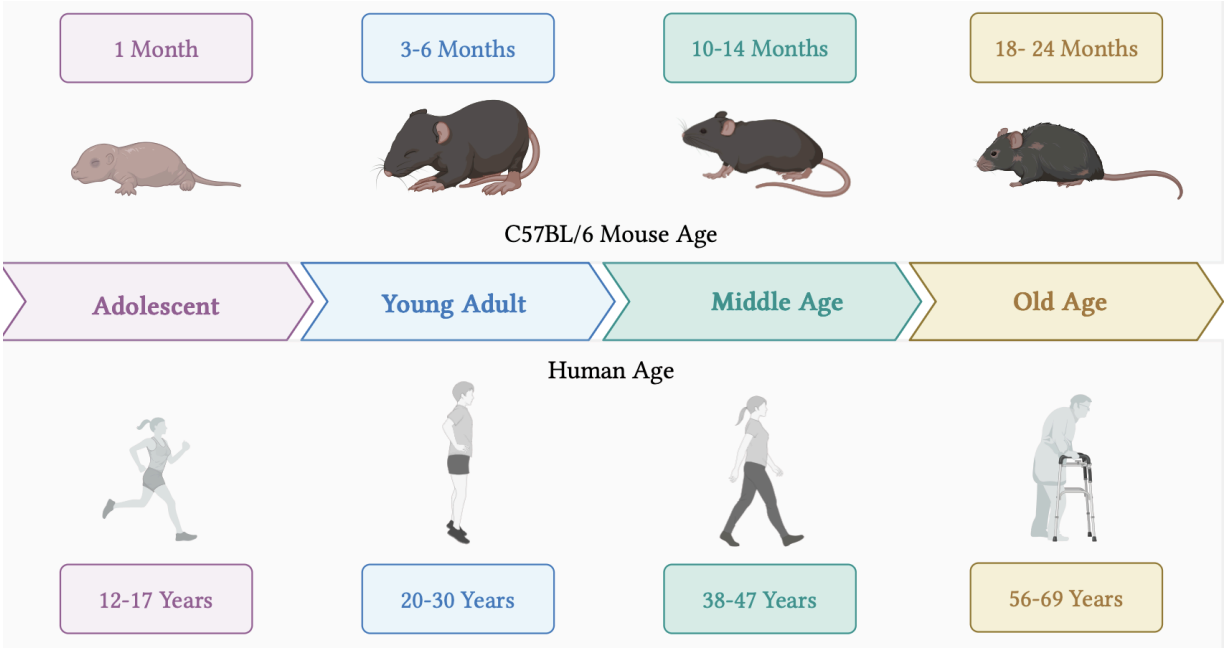

Figure 2. Timeline comparing C57BL/6J mouse age in months to approximate human age equivalents in years. The study window (18 to 24-25 months, corresponding to approximately 56 to 69 human years) is highlighted, representing the transition from middle age to early old age. Human age equivalents adapted from Flurkey et al. (2007).

At 18 months of age, C57BL/6J mice exhibit sufficient heterogeneity in wound healing responses to enable stratification into fast and slow healers, while remaining young enough that identified mechanisms could potentially be targeted to alter subsequent aging trajectories. The period from 18 to 24-25 months in mice approximates the transition from middle age to early old age in humans, roughly corresponding to ages 56 to 69 years (Flurkey et al., 2007). This represents a critical window when resilience differences become manifest before irreversible functional decline occurs.

This study builds upon preliminary findings to provide comprehensive characterization of wound healing as a predictive biomarker of aging resilience. Our central hypothesis posits that aged mice with superior wound healing capacity will demonstrate enhanced physiological and

cognitive resilience compared to poor healers, accompanied by distinct transcriptomic signatures predictive of aging outcomes. To test this hypothesis, a longitudinal cohort design stratifying mice based on wound healing response is employed, followed by comprehensive behavioral phenotyping and unbiased transcriptomic profiling across multiple tissues. Two specific objectives guide this research. First, we determined the relationship between wound healing capacity and physiological resilience markers across motor function, cognitive performance, body composition, and organ pathology in aging mice. Second, we characterized transcriptomic and molecular correlates of wound healing response phenotypes using unbiased RNA sequencing across hippocampus and liver, followed by targeted immunohistochemical assessment of neuroplasticity, synaptic integrity, and neuroinflammatory markers in brain tissue. This research will establish wound healing capacity as a validated biomarker for aging resilience, identify transcriptomic signatures of resilient aging phenotypes, and generate comprehensive datasets documenting relationships between early physiological responses and later functional outcomes. Ultimately, identified molecular pathways will inform the design of interventions to enhance resilience in vulnerable individuals and promote healthy longevity.

Materials and Methods

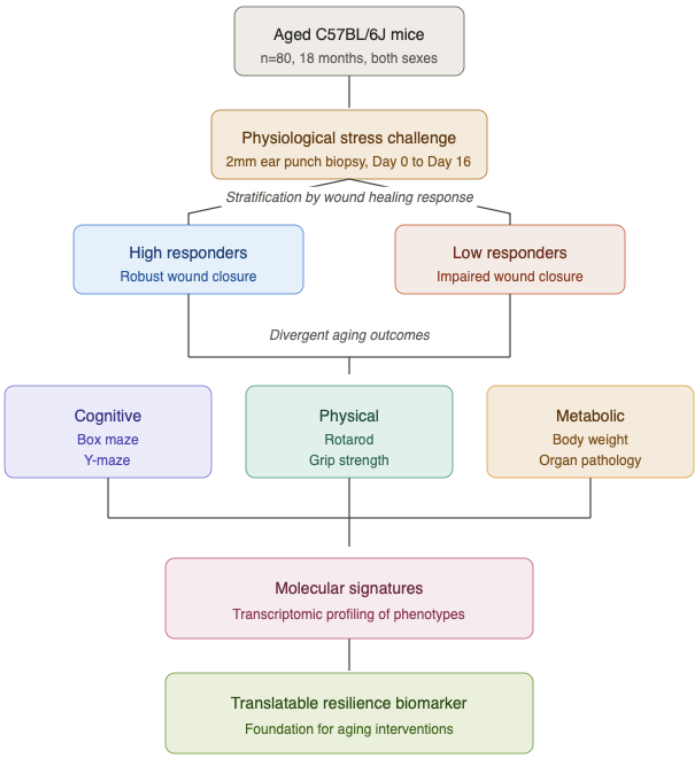

Figure 3. Study design schematic for wound healing resilience study. Aged C57BL/6J mice (n=80, 18 months, both sexes) underwent a standardized 2mm ear punch biopsy and were stratified by wound closure response at Day 16 into high responders and low responders. Both cohorts were assessed across cognitive, physical, and molecular domains at 24-25 months, followed by transcriptomic profiling to identify molecular signatures of resilient aging phenotypes.

Mice. This study used 80 C57BL/6J mice (40 male, 40 female) obtained from the National Institute of Aging Aged Rodent Colony at 18 months of age. Mice were housed in a pathogen-free facility with a 14:10 light:dark cycle, with standard chow diet and water provided ad libitum. All procedures were approved by the University of Washington Institutional Animal Care and Use Committee (IACUC). Upon arrival, mice underwent a two-week acclimation period before any experimental procedures were initiated. Following acclimation, all mice received a 2mm ear punch for identification purposes. Body weights were measured weekly throughout the study duration, and cage changes were performed every other week. Body weight and tumor incidence were monitored as general health parameters throughout the longitudinal study period.

Figure 4. Wound healing assessment methodology. A. Photograph of mouse pinna with 2mm ear punch wound at Day 0. B. Close-up of fresh wound immediately post-biopsy (Day 0). C. Representative high responder ear at Day 16 showing near-complete wound closure. Wound closure was calculated as: [(Day 0 area - Day 16 area) / Day 0 area] x 100.

Wound Healing Assessment. Wound healing capacity was assessed using a standardized 2mm ear punch biopsy performed at 18 months of age. The procedure was conducted using a sterile 2mm biopsy punch on the pinna of the ear. Immediately following the procedure at day 0 and at day 16 post-biopsy, the wound site was photographed under standardized conditions using consistent lighting and camera positioning. Digital photographs were captured at a fixed distance to ensure reproducibility of measurements. Wound area was quantified using ImageJ software (National Institutes of Health). For each image, the wound perimeter was manually traced and the enclosed area calculated in square millimeters. Wound closure percentage was calculated using the formula: [(initial area − day 16 area) / initial area] × 100. Quality control measures included standardized photography conditions, blinded image analysis to prevent observer bias, and validation of measurement reproducibility through repeat measurements on a subset of images. Based on the distribution of healing responses, mice were stratified into high responders and low responders using the median wound closure percentage at day 16 as the division criterion, resulting in an initial stratification of n=20 per group per sex prior to longitudinal attrition and exclusion of the negative healing phenotype.

Longitudinal Health Monitoring. Following wound healing assessment and stratification, mice were monitored longitudinally from 18 to 25 months of age. Body weight was measured weekly to track age-related changes in body mass and identify potential health concerns. Mice were visually inspected during weekly weighing for signs of tumor development, with any palpable masses or visible abnormalities documented. General health assessments including posture, grooming, activity level, and responsiveness were conducted during routine husbandry to identify mice requiring veterinary attention or removal from the study.

Behavioral Testing. Comprehensive behavioral testing was conducted when mice reached 24 to 25 months of age to assess cognitive and physical function across multiple domains. All behavioral assessments were performed during the light phase of the light:dark cycle. Testing was conducted over a two-week period following a standardized schedule to minimize stress and allow adequate rest between assessments. Week 1 consisted of box maze testing followed by grip

strength assessment. Week 2 consisted of Y-maze testing followed by rotarod assessment. All behavioral testing equipment was cleaned with 70% ethanol between individual mice and thoroughly cleaned between cages to minimize olfactory cues.

Box Maze. Spatial navigation learning and memory were assessed using the box maze behavioral paradigm, a validated cognitive assessment for aged mice (Darvas et al., 2020). The apparatus consists of a large box with reflective material lining the interior walls. Eight holes are evenly distributed around the perimeter of the maze floor. Seven holes serve as false exits, sealed with PVC caps, while one hole serves as the true exit connected via PVC piping to a dark rest cage. The maze interior is brightly illuminated from above with an LED light to provide a mild aversive stimulus motivating escape behavior. A small visual cue was positioned above the exit hole to facilitate spatial orientation.

Individual mice were tested in four consecutive trials with inter-trial intervals. Each trial began with placement of the mouse in the center of the maze, facing a different direction, allowing 120 seconds to locate and enter the true exit. Entry into false escapes was defined as the mouse's head and two paws entering the PVC tube. Mice that did not successfully escape within 120 seconds were gently guided to the exit by the investigator. Upon entry, mice remained in the dark rest cage for 30 seconds before returning to the home cage for a 90-second inter-trial interval. Performance was recorded across four trials. Between trials, the maze and rest cage were cleaned with 70% ethanol. Between cages, all equipment was thoroughly sprayed with 70% ethanol and allowed to dry completely.

Cognitive performance was assessed using the Learning Index, a weighted metric normalizing for population-wide variance, calculated as described (Darvas et al., 2020). For each mouse, performance time for trials 2, 3, and 4 was divided by the performance time of trial 1, subtracted by 1, then multiplied by the respective trial variance ratio. Output values for trials 2, 3, and 4 were summed to generate the Learning Index, where higher values indicate superior learning capability and cognitive function.

Y-Maze Spontaneous Alternation. Spatial working memory was assessed using the Y-maze spontaneous alternation test, exploiting the innate tendency of rodents to explore novel environments (Kraeuter et al., 2019). The apparatus consists of three identical arms constructed of opaque plastic and arranged in a Y-configuration with 120-degree angles between arms. Each mouse was placed in one arm and allowed to freely explore for 5 minutes, with arm entries recorded in real-time. An entry was defined as all four paws entering an arm. Spontaneous alternation percentage was calculated as: (number of triads containing entries into all three different arms / total possible alternations) × 100, where total possible alternations equals total entries minus 2. Higher alternation percentages indicate superior spatial working memory. Between mice, the maze was thoroughly cleaned with 70% ethanol and dried to eliminate olfactory cues.

Rotarod. Motor coordination, balance, and motor learning were assessed using the accelerating rotarod test, a standard measure of motor function in rodent aging studies (Shiotsuki et al., 2010). The apparatus consists of a rotating rod suspended above a padded landing platform. Mice first underwent a habituation session during which they were placed on the stationary rod till they

fell. On the testing day, the rod accelerated linearly. Latency to fall was automatically recorded in seconds. Mice completed three trials with inter-trial rest intervals, and performance was measured as the average latency to fall across trials. Longer latencies indicate superior motor coordination and balance. The rod was cleaned with 70% ethanol between mice.

Grip Strength. Forelimb muscle strength and neuromuscular function were quantified using a grip strength meter (San Diego Instruments), a standard assessment of physical function in aging rodents (Shiotsuki et al., 2010). Mice were held by the tail and positioned to grasp a metal grid connected to a force transducer. Once a firm grip was established, mice were pulled horizontally at a steady, gentle rate until grip was released, and peak force was recorded. Each mouse performed five consecutive trials with approximately 30-second inter-trial intervals. The highest value was excluded as a potential outlier, and the remaining four values were averaged to generate the grip strength score. Higher values indicate greater forelimb muscle strength. The grid was cleaned with 70% ethanol between mice.

Tissue Collection. Within one week of completing behavioral assessment, mice were euthanized by carbon dioxide asphyxiation followed by decapitation. Brain and major organs were harvested immediately. Brains were rapidly removed and bisected along the midline. One hemisphere was immersion-fixed in 10% neutral buffered formalin (NBF) for 72 hours at room temperature, then transferred to 70% ethanol until processing for immunohistochemistry. The contralateral hemisphere was microdissected on ice to isolate the hippocampus. Liver tissue was also collected during necropsy. Dissected tissues were flash-frozen in liquid nitrogen and stored at -80°C until RNA extraction. Major organs including heart, lungs, kidneys, and spleen were collected and either flash-frozen or fixed in 10% NBF following the same protocols, and are archived for future analyses beyond the scope of the current study.

Immunohistochemistry. Fixed brain hemispheres were processed by the Ladiges Laboratory Histology Core. Tissues were dehydrated through graded alcohols, cleared in xylene, and embedded in paraffin wax blocks. Embedded brains were sectioned sagittally at 4 μm thickness and mounted on positively charged glass slides.

For immunohistochemical staining, slides underwent deparaffinization and rehydration by sequential immersion in xylene, 100% ethanol, 95% ethanol, 70% ethanol, and deionized water. Heat-induced antigen retrieval was performed by immersing slides in citrate pH 6.0 and heating in a water bath at 98°C for 20 minutes. After cooling to room temperature, a hydrophobic barrier was applied around tissue sections using a PAP pen.

Primary antibody staining was performed using the markers listed in Table 1. For rabbit primary antibodies (BDNF, IBA1, GFAP), detection was performed using the Abcam DAB Rabbit kit (ab64261) according to the manufacturer's instructions. Endogenous peroxidase activity was blocked by incubation with 3% hydrogen peroxide for 10 minutes, followed by three washes in Tris-buffered saline with 0.1% Tween-20 (TBST). Slides were incubated with protein block for 10 minutes to reduce non-specific binding, washed three times in TBST, then incubated overnight at 4°C with primary antibody diluted in TBST.

Following overnight primary antibody incubation, slides were washed three times in TBST and incubated with the appropriate biotinylated secondary antibody for 10 minutes. After three additional TBST washes, slides were incubated with streptavidin-conjugated horseradish peroxidase for 10 minutes. Chromogenic detection was performed using DAB chromogen diluted in DAB substrate buffer until optimal color development, monitored microscopically. Reactions were stopped in deionized water. Slides were counterstained with hematoxylin, dehydrated through graded alcohols, cleared in xylene, and coverslipped using permanent mounting medium.

For general histopathological assessment, additional sections from brain, heart, liver, kidney, and pancreas were stained with hematoxylin and eosin (H&E) using standard protocols to evaluate overall tissue morphology and identify pathological changes including fibrosis, inflammation, and necrosis. Histopathological evaluation of peripheral organ sections was performed by a board-certified veterinary pathologist (J.M. Snyder, DVM, MS, DACVP). Lesions were scored semiquantitatively using standardized criteria for each organ. In the liver, scoring categories included hepatic degeneration and necrosis (0-4), hepatic lipidosis (0-4), periportal inflammation (0-4), bile duct hyperplasia and cysts (0-4), lymphoid aggregates (0-4), microgranulomas (0-4), Ito cell hyperplasia (0-1), telangiectasia (0-1), and neoplasia (0-2). In the kidney, scoring categories included nephropathy (0-4), pyelonephritis (0-4), infarcts (0-1), lymphoid accumulations (0-4), mineralization (0-1), amyloid deposition (0-1), and neoplasia (0-2). In the heart, scoring categories included cardiomyopathy (0-4), arteriosclerosis (0-4), myocardial inflammation (0-4), and lymphoid accumulations (0-4). In the pancreas, scoring categories included exocrine atrophy (0-4), chronic pancreatitis (0-4), fatty infiltration (0-4), lymphoid accumulations (0-4), islet hyperplasia (0-1), and neoplasia (0-2). For all organs, a score of 0 indicates absence of the lesion, with higher scores reflecting increasing severity or extent as defined by standardized morphological criteria. Scores were compared between high and low wound healing responder groups using the Mann-Whitney U test, appropriate for ordinal data.

Table 1. Primary antibodies used for immunohistochemical analysis of brain tissue.

Target	Host	Catalog No.	Supplier	Dilution
BDNF	Rabbit	ab213323	Abcam	1:100
Synaptophysin	Rabbit	MA5-16402	Thermo Fisher	1:250
IBA1	Rabbit	ab178846	Abcam	1:1000
GFAP	Rabbit	PA1-10019	Thermo Fisher	1:1500

Image Acquisition and Analysis. Stained slides were imaged using a Nikon NIS-D microscope at 20× magnification. Representative images of the hippocampus and cerebellum were captured under standardized lighting and exposure conditions for each mouse. Digital images were analyzed using QuPath software (version 0.5.1) to calculate the percentage of tissue area with positive DAB staining as the primary measure of protein expression. All image analysis was performed by investigators blinded to mouse identity and experimental group.

RNA Sequencing. Total RNA was extracted from flash-frozen hippocampus and liver tissues stored at -80°C. Sixteen samples were selected for RNA sequencing, with n=4 per group

representing high responder males and low responder males. Sample selection was not based on wound healing alone; rather, mice were selected based on composite overall performance across all behavioral and physiological measures collected in this study, including wound healing percent closure, learning index, grip strength, rotarod latency to fall, and Y-maze percent alternation. For each measure, mice were ranked and assigned to quartiles. High responder RNA-seq mice were selected from among males in the top quartile of overall composite performance, and low responder RNA-seq mice were selected from among males in the bottom quartile. This approach ensured that sequenced animals represented genuinely extreme overall aging phenotypes rather than outliers on any single metric. Final selection was confirmed with RNA quality assessment, with only samples achieving acceptable purity and integrity proceeding to library preparation. Frozen tissues were homogenized in TRIzol reagent using a bead mill homogenizer with ceramic beads. Following homogenization, samples were centrifuged at 12,000 × g for 10 minutes at 4°C, and the supernatant was transferred to new tubes.

RNA isolation proceeded using a standard TRIzol-chloroform extraction protocol. Chloroform was added at 0.2 mL per 1 mL TRIzol, samples were mixed vigorously, incubated for 3 minutes at room temperature, and centrifuged at 12,000 × g for 15 minutes at 4°C. The aqueous phase was transferred and RNA precipitated by adding isopropanol at 0.5 mL per 1 mL TRIzol for 10 minutes at room temperature. RNA was pelleted by centrifugation at 12,000 × g for 10 minutes at 4°C, washed twice with 75% ethanol, air-dried for 10 minutes, and resuspended in 50 µL nuclease-free water (Qiagen 1039480). Concentration and purity were assessed using a NanoDrop spectrophotometer, with acceptable A260/A280 ratios of 1.8 to 2.0 and A260/A230 ratios of 1.8 to 2.2.

Additional purification was performed using the RNeasy Mini Kit (Qiagen 74104). Samples were applied to RNeasy spin columns, washed sequentially with RW1 and RPE buffers, and eluted in 30 µL nuclease-free water. Purified RNA was stored at -80°C and shipped on dry ice to Novogene Corporation for quality control and sequencing. RNA integrity was assessed using the Agilent Bioanalyzer system, with only samples achieving a RNA Integrity Number (RIN) ≥ 7.0 proceeding to library preparation. Sequencing libraries were prepared using standard poly(A) selection and strand-specific library construction protocols. Paired-end sequencing was performed on the Illumina NovaSeq X Plus platform targeting 40 million read pairs per sample.

Bioinformatic Analysis. All bioinformatic analyses were performed in Python (v3.12.3) using Visual Studio Code (v1.119.1) on WSL Ubuntu (v24.02.2). Paired-end FASTQ files delivered by Novogene Corporation were processed using Pyrpipe (v0.0.5), an RNA-seq workflow management package (Singh et al., 2021). Pyrpipe coordinated adapter and quality trimming using Trim-galore (v0.6.10), alignment to the C57BL/6J reference genome (GRCm39; NCBI assembly GCF_000001635.27) using STAR (v2.7.11b), transcript assembly using StringTie (v3.0.0), and transcript-level quantification using Salmon (v1.10.3). All reference genome and annotation files were obtained from the NCBI database.
Differential expression analysis was performed separately for hippocampus and liver using PyDESeq2 (v0.5.1), a Python implementation of the DESeq2 pipeline (Muzellec et al., 2023). Transcript-level quantification files generated by Salmon were converted to gene-level counts using pytximport (v0.12.0), which generated a transcript-to-gene mapping key from the same GRCm39 annotation file used in the Pyrpipe workflow. Genes with total counts fewer than 10

across all samples were excluded prior to statistical testing. All differential expression statistics, including Wald test statistics and Benjamini-Hochberg false discovery rate correction, were performed using built-in PyDESeq2 methods. Genes with a Benjamini-Hochberg adjusted p-value (padj) < 0.05 were considered differentially expressed.

Gene set enrichment analysis was performed using the GSEA desktop application (v4.4.0; Subramanian et al., 2005; Mootha et al., 2003). The mouse Hallmark gene sets collection (mh.all.v2026.1.Mm.symbols) was obtained from the MSigDB database. A ranked gene list was generated for each tissue by ordering all expressed genes by their PyDESeq2 Wald statistic, with positive values indicating higher expression in high responders. All GSEA runs completed without error as indicated by the application status field. Pathways with FDR < 0.25 were considered for biological interpretation, consistent with GSEA reporting conventions, with FDR < 0.05 denoting statistical significance.

Statistical Analysis. All statistical analyses, graphs, and p-values were generated using GraphPad Prism (version 10.2.3). Statistical significance was defined as alpha < 0.05 for all behavioral, physiological, and histological comparisons. Mice exhibiting wound healing values below -10% (indicating net wound area enlargement at Day 16 relative to Day 0) were designated as exhibiting a negative healing phenotype and excluded from primary correlation and group comparison analyses. This threshold was selected based on the biological rationale that net wound enlargement represents a qualitatively distinct healing response, characterized by tissue dysregulation or failed repair initiation, rather than the lower end of a normal healing continuum. Wound healing requires coordinated immune activation, angiogenesis, and cellular proliferation (Broughton et al., 2006); net wound enlargement suggests a fundamental disruption of these processes inconsistent with variation in healing capacity. Animals meeting this criterion (n = 10) were not included in RNA sequencing analyses. A secondary descriptive analysis of this subgroup is reported in the Results. To empirically validate the exclusion of negative healers as a biologically distinct subgroup, Kruskal-Wallis one-way analysis of variance was used to compare functional outcomes across three groups: negative healers, low responders, and high responders. This non-parametric test was selected because it does not assume normality and is appropriate for comparing three independent groups on continuous outcome measures. For continuous behavioral and histological outcome measures, Spearman's rank correlation was used to evaluate the relationship between wound healing capacity and each outcome variable, reported separately for the full filtered cohort and for sex-stratified subgroups. Group comparisons between high and low wound healing responders were performed using unpaired t-tests with Welch's correction to account for potential inequality of variance between groups, with groups defined by the median wound closure percentage at Day 16 (27.05%). For ordinal histopathological scoring data, the Mann-Whitney U test was used as a non-parametric alternative.

Results

Wound healing capacity varied substantially among aged C57BL/6J mice. Wound closure percentage across the cohort ranged from -79.7% to 88.1%, demonstrating substantial natural variation in healing capacity among genetically homogeneous mice maintained under identical environmental conditions. A median wound closure of 27.05% was used to stratify mice into high responders (closure ≥ 27.05%, n=28) and low responders (closure < 27.05%, n=28) for subsequent analyses (Figure 5). Ten mice exhibited wound healing values below -10%, indicating net wound area enlargement at Day 16, and were excluded from primary correlation and group comparison analyses. This threshold was selected on the basis that net wound enlargement represents a qualitatively distinct healing response, reflecting tissue dysregulation or failed repair initiation rather than the lower end of a normal healing continuum; these animals were also not included in RNA sequencing analyses. A secondary descriptive analysis of this subgroup is reported below. Of the 80 mice that completed wound healing assessment, 66 survived to behavioral testing at 24 to 25 months of age, with 14 mice removed from the study due to death, spontaneous tumor development, or deteriorating health. Tumor incidence and general health decline were monitored throughout as indicators of study attrition rather than primary outcomes, and were not systematically associated with wound healing phenotype.

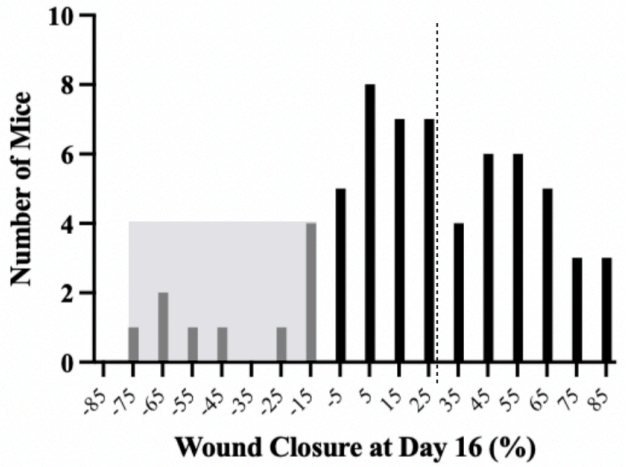

Figure 5. Wound healing distribution in aged C57BL/6J mice. Frequency distribution of wound closure percentage at Day 16 for all mice completing behavioral testing (n=66). The median wound closure of 27.05% was used to stratify mice into high responders (n=28) and low responders (n=28). Ten mice with wound healing below -10% (shaded region) were designated as a negative healing phenotype and excluded from primary analyses; these animals are shown for reference.

Mice with wound healing below -10% do not represent the lower end of a continuous healing-to-function spectrum. To characterize animals exhibiting net wound enlargement, the 10 excluded mice were compared to moderate healers (-10% to 50%) and positive healers (≥50%) using Kruskal-Wallis tests across all four functional outcomes. No significant differences were detected for learning index ($H = 2.12$, $p = 0.346$), Y-maze alternation ($H = 0.62$, $p = 0.734$), grip strength ($H = 0.59$, $p = 0.743$), or rotarod performance ($H = 3.25$, $p = 0.197$). Pairwise

comparisons between negative healers and both moderate and positive healer groups were similarly non-significant. Notably, negative healers did not perform worse than other groups on any measure, suggesting that animals with extreme negative wound healing represent a biologically distinct subgroup whose functional outcomes are decoupled from their wound healing response rather than simply the worst performers on a resilience continuum.

Body weight was comparable between high and low responders throughout the study. Body weight was monitored weekly to evaluate longitudinal health trajectories and confirm that healing-based stratification did not reflect pre-existing differences in general health. At the time of wound healing assessment (18 months), body weight was comparable between high and low responders in both males and females. No meaningful divergence in body mass between groups was observed over the course of the study, indicating that stratification reflected wound healing capacity specifically rather than overall body condition.

Comprehensive behavioral assessment was conducted at 24 to 25 months of age across four assays evaluating cognitive and physical function. Spearman's rank correlations were used to evaluate the relationship between wound healing capacity (percent closure at Day 16) and each continuous outcome variable. Unpaired t-tests with Welch's correction were used to compare high and low responders stratified by median wound closure. Results are reported for the 56 mice that completed behavioral testing after exclusion of the 10 negative healers.

High and low wound healing responders did not differ significantly on box maze learning index (Figure 6). Spearman's correlation between wound healing capacity and learning index was weak and non-significant in the full filtered cohort ($r_s = -0.175$, $p = 0.197$, $n = 56$) and in sex-stratified analyses (females: $r_s = -0.222$, $p = 0.230$, $n = 31$; males: $r_s = -0.075$, $p = 0.720$, $n = 25$). Group comparisons between high and low responders likewise showed no significant difference (high: 1.20 ± 0.71; low: 1.43 ± 0.71; $t = 1.212$, $df = 52.84$, $p = 0.231$). Both groups completed the maze task and showed comparable performance across trials.

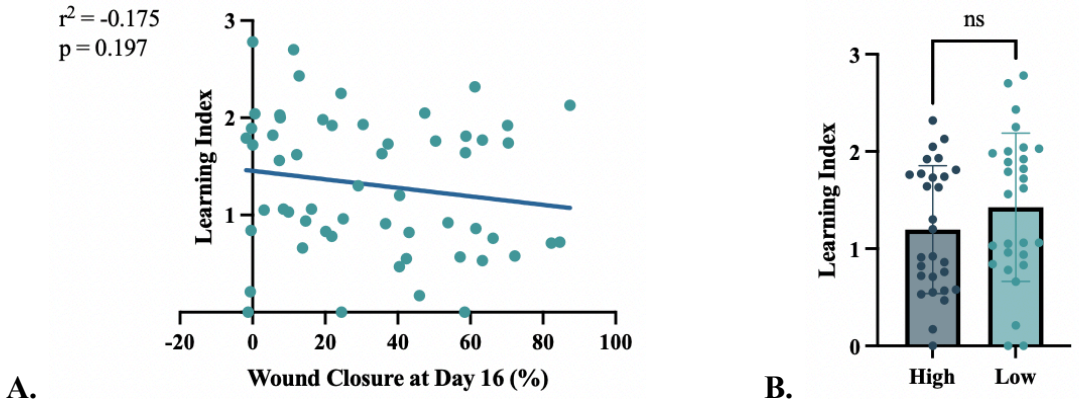

Figure 6. Box maze learning index in wound healing responder mice. A. Scatter plot of wound healing percent closure at Day 16 versus learning index score for all mice in the filtered cohort (n=56), with Spearman correlation line shown ($r_s = -0.175$, $p = 0.197$). B. Comparison of learning index score between high (n=28) and low (n=28) responders defined by median split. ns = not significant by unpaired t-test with Welch's correction. Data presented as mean ± SD.

High and low wound healing responders did not differ significantly on Y-maze spontaneous alternation (Figure 7). In the full filtered cohort, Spearman's correlation between wound healing capacity and Y-maze percent alternation was non-significant (rs = 0.041, p = 0.763, n = 56). Sex-stratified analyses likewise revealed no significant associations in females (rs = -0.120, p = 0.520, n = 31) or males (rs = 0.100, p = 0.634, n = 25). Group comparisons between high and low responders showed no significant difference (high: 60.07 ± 12.80%; low: 60.91 ± 12.80%; t = 0.248, df = 43.85, p = 0.805). Both groups performed above the 50% chance threshold, indicating intact spatial working memory overall.

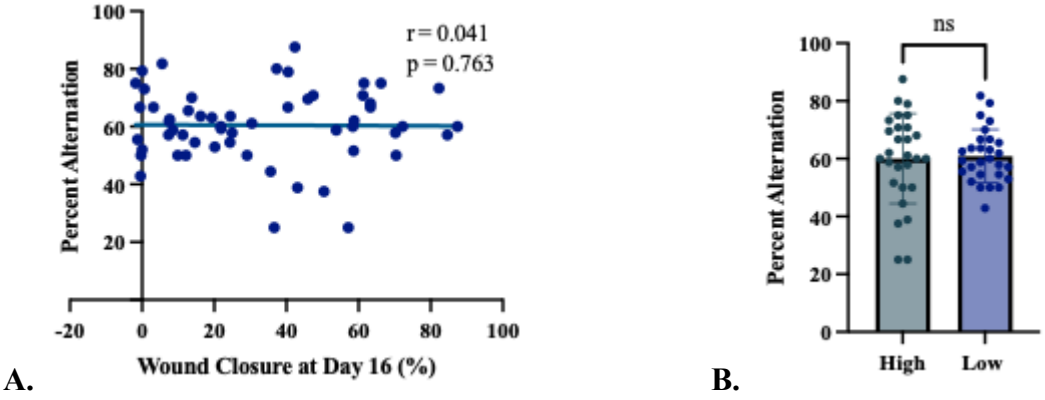

Figure 7. Y-maze spontaneous alternation in wound healing responder mice. A. Scatter plot of wound healing percent closure at Day 16 versus spontaneous alternation percentage for the filtered cohort (n=56), with Spearman correlation line shown (rs = 0.041, p = 0.763). Dashed line indicates 50% chance performance. B. Comparison of spontaneous alternation percentage between high (n=28) and low (n=28) responders defined by median split. ns = not significant by unpaired t-test with Welch's correction. Data presented as mean ± SD.

High and low wound healing responders did not differ significantly on forelimb grip strength (Figure 8). Grip strength was measured as an index of neuromuscular function and physical resilience. Spearman's correlation between wound healing capacity and grip strength was non-significant in the full filtered cohort (rs = -0.218, p = 0.107, n = 56) and in sex-stratified analyses (females: rs = -0.256, p = 0.165, n = 31; males: rs = -0.172, p = 0.413, n = 25). Group comparisons between high and low responders were likewise non-significant (high: 2.80 ± 0.54 N; low: 2.99 ± 0.54 N; t = 1.279, df = 54.00, p = 0.206).

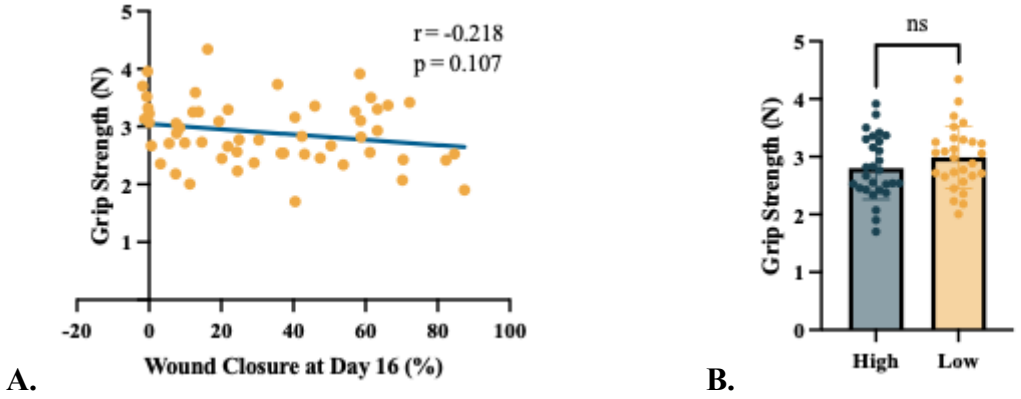

Figure 8. Forelimb grip strength in wound healing responder mice. A. Scatter plot of wound healing percent closure at Day 16 versus peak forelimb force (Newtons) for the filtered cohort (n=56), with Spearman correlation line shown (rs = -0.218, p = 0.107). B. Comparison of grip strength between high (n=28) and low (n=28) responders defined by median split. ns = not significant by unpaired t-test with Welch's correction. Data presented as mean ± SD.

Rotarod performance was significantly greater in high wound healing responders compared to low responders (Figure 9). Motor coordination, balance, and motor learning were evaluated using the accelerating rotarod. In the full filtered cohort, wound healing capacity showed a positive trend with rotarod performance that approached significance (rs = 0.223, p = 0.098, n = 56). Group comparisons confirmed a significant difference between high and low responders (high: 133.20 ± 33.53 sec; low: 112.50 ± 33.53 sec; t = 2.309, df = 50.13, p = 0.025). Sex-stratified analysis revealed the most robust finding in the dataset: wound healing capacity was significantly positively correlated with rotarod performance in male mice (rs = 0.575, p = 0.003, n = 25), and high-healing males demonstrated substantially longer latency to fall than low-healing males (high: 141.80 ± 34.75 sec; low: 105.70 ± 34.75 sec; t = 2.597, df = 21.42, p = 0.017). This association was not observed in female mice (rs = -0.025, p = 0.939, n = 31). Of the four behavioral assays administered, rotarod showed the most consistent and significant evidence of a wound healing-motor resilience relationship across the full cohort and within the male sex.

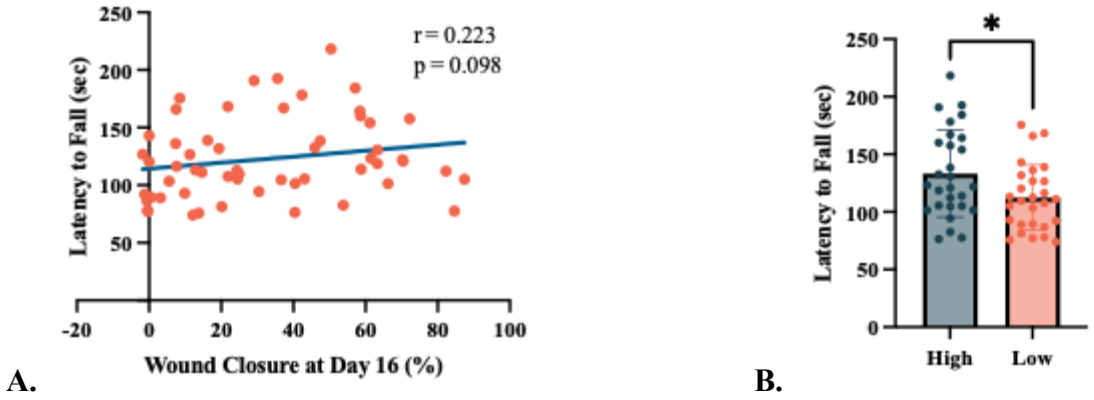

Figure 9. Rotarod performance in wound healing responder mice. A. Scatter plot of wound healing percent closure at Day 16 versus latency to fall (seconds) for the filtered cohort (n=56), with Spearman correlation line shown (rs = 0.223, p = 0.098). B. Comparison of latency to fall between high (n=28) and low (n=28) responders defined by median split. *p = 0.025 by unpaired t-test with Welch's correction. Data presented as mean ± SD. See Figure 10 for sex-stratified analysis.

Sex-stratified analysis revealed a significant association between wound healing capacity and rotarod performance in male mice (Figure 10). When behavioral data were analyzed separately by sex in the filtered cohort, a significant association between wound healing capacity and rotarod performance emerged in males (rs = 0.575, p = 0.003; t = 2.597, df = 21.42, p = 0.017), with high-healing males demonstrating substantially longer latency to fall than low-healing males (high: 141.80 ± 34.75 sec; low: 105.70 ± 34.75 sec; t = 2.597, df = 21.42, p = 0.017). This association was not observed in female mice (rs = -0.025, p = 0.939, n = 31), indicating a male-specific association between wound healing capacity and motor coordination performance.

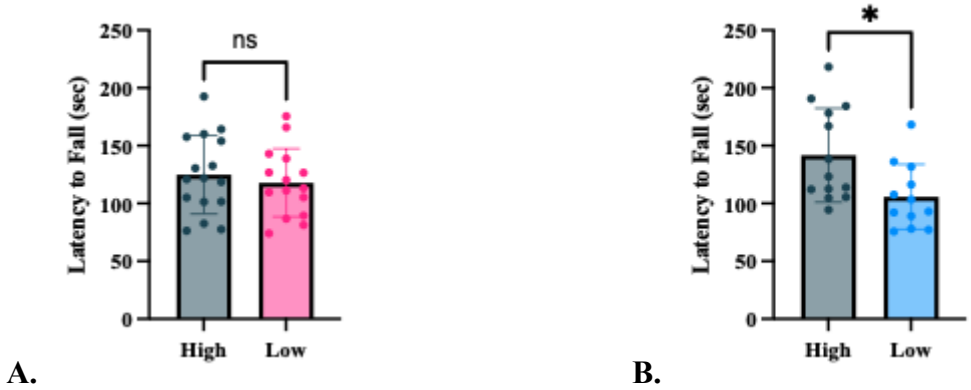

Figure 10. Sex-stratified rotarod performance in wound healing responder mice. Latency to fall (seconds) shown separately for females (A) and males (B). High and low responder groups defined by median wound closure within each sex. A. In females, no significant difference was observed. *p < 0.05, ns = not significant by unpaired t-test with Welch's correction. B. In males, high healers (141.80 ± 34.75 sec) significantly outperformed low healers (105.70 ± 34.75 sec). Data presented as mean ± SD. Analysis is exploratory; no correction for multiple comparisons was applied.

No significant sex-specific associations were identified for learning index, Y-maze alternation, or grip strength in either sex. These analyses are exploratory given the reduced sample sizes within each sex (females: n = 31; males: n = 25) and should be interpreted as hypothesis-generating pending replication in a larger cohort. No correction for multiple comparisons was applied.

Immunohistochemical analysis of brain tissue was performed to characterize protein expression of markers associated with synaptic integrity, neuroplasticity, and neuroinflammatory status. General histopathological assessment was conducted in brain and peripheral organs via hematoxylin and eosin staining.

Brain sections were stained for BDNF, synaptophysin, GFAP, and IBA1 to characterize neuroplasticity, synaptic integrity, and neuroinflammatory status in the hippocampus and cerebellum. Staining was performed using the Abcam DAB Rabbit detection system with citrate antigen retrieval.

Brain-Derived Neurotropic Factor (BDNF) expression was quantified by percent area positive staining in hippocampus and cerebellum in the filtered cohort (Figure 11). High and low responders demonstrated comparable BDNF immunoreactivity in both brain regions. In hippocampus, Spearman's correlation between wound healing capacity and BDNF was non-significant in the full filtered cohort (rs = -0.046, p = 0.739, n = 56), and group comparisons showed no significant difference between high and low responders (high: 0.40 ± 0.23%; low: 0.42 ± 0.29%; U = 398.0, p = 0.928). Sex-stratified analyses likewise revealed no significant associations in females (rs = -0.031, p = 0.869, n = 31; t = -0.337, df = 28.6, p = 0.739) or males (rs = -0.219, p = 0.294, n = 25; t = -0.048, df = 22.8, p = 0.962). Cerebellar BDNF expression was similarly comparable between groups (rs = 0.083, p = 0.563, n = 51; U = 338.0, p = 0.814). BDNF is a neurotrophin critical for hippocampal synaptic plasticity, long-term potentiation, and cognitive function (Bekinschtein et al., 2008).

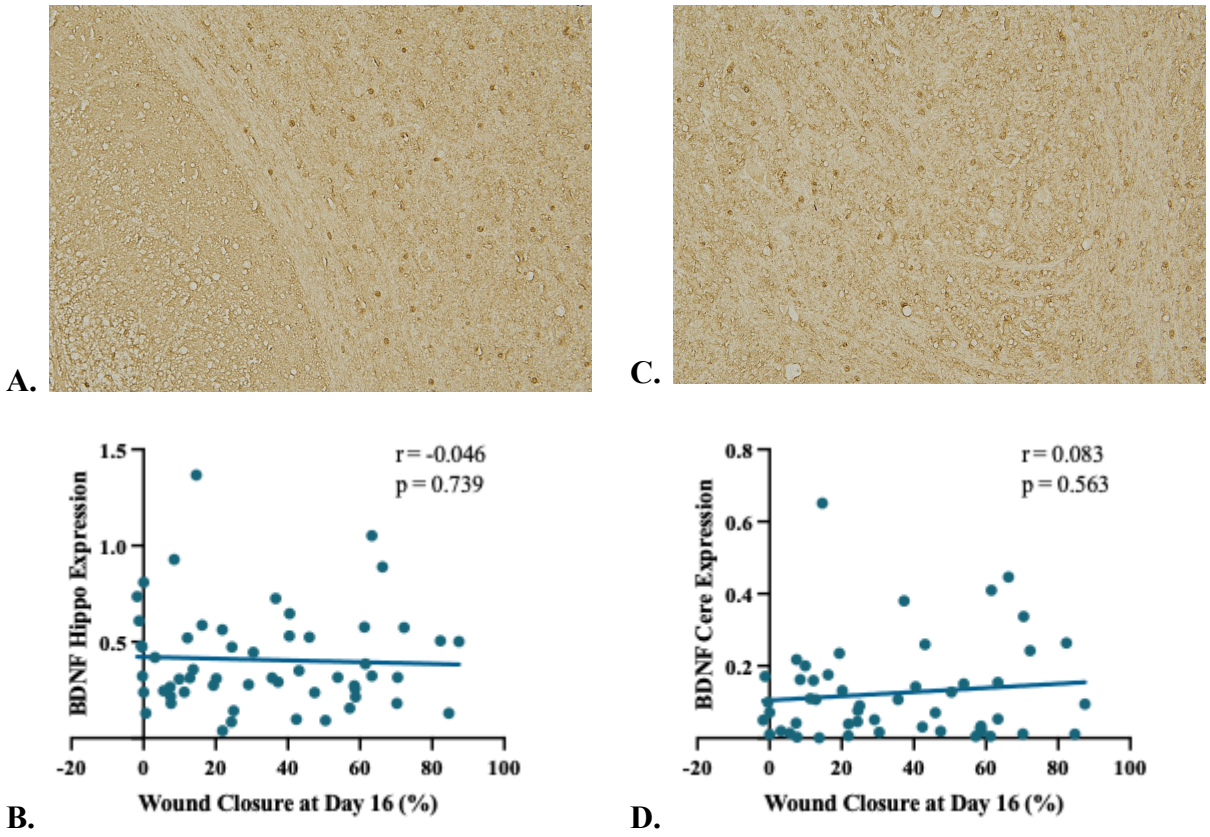

Figure 11. BDNF immunostaining in wound healing responder mice. A. Representative 20x hippocampus image. B. Scatter plot of wound healing percent closure at Day 16 versus BDNF percent area positive staining in the hippocampus for the filtered cohort (n=56), with Spearman correlation line shown (rs = -0.046, p = 0.739). C. Representative 20x cerebellum image. D. Scatter plot of wound healing percent closure at Day 16 versus BDNF percent area positive staining in the cerebellum (n=51), with Spearman correlation line shown (rs = 0.083, p = 0.563). ns = not significant.

Synaptophysin expression, a marker of pre-synaptic vesicle density and a proxy for synaptic integrity, was quantified in hippocampus and cerebellum (Figure 12). High and low responders demonstrated comparable synaptophysin staining in both regions. In hippocampus, Spearman's correlation between wound healing and synaptophysin was non-significant (rs =

0.047, p = 0.772, n = 41), and group comparisons showed no significant difference (high: 2.55 ± 1.97%; low: 2.24 ± 1.97%; t = 0.503, df = 38.80, p = 0.618). Cerebellar synaptophysin was similarly comparable between groups (rs = 0.032, p = 0.849, n = 38; t = 0.191, df = 35.49, p = 0.849). Synaptophysin levels correlate with cognitive performance in aging rodent models and reflect the maintenance of functional synaptic contacts in hippocampal circuits (Smith et al., 2000).

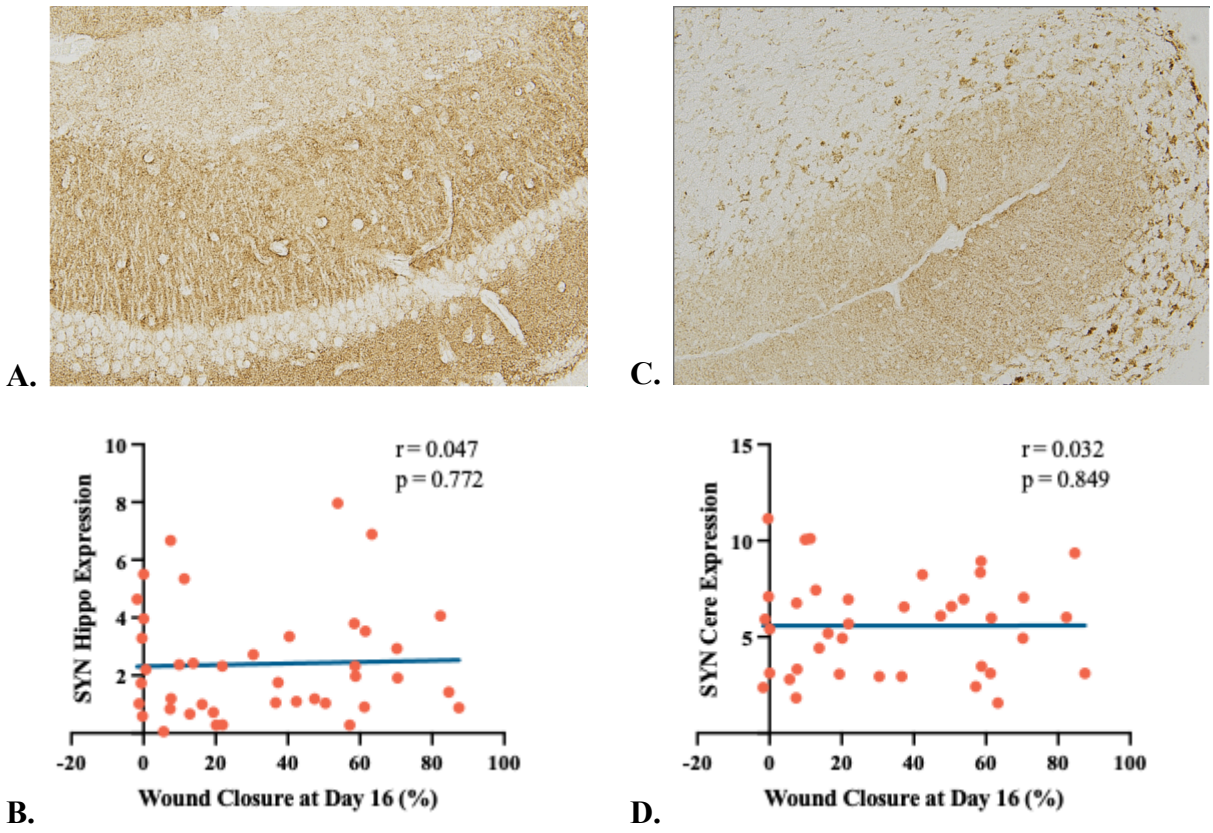

Figure 12. Synaptophysin immunostaining in wound healing responder mice. A. Representative 20x hippocampus image. B. Scatter plot of wound healing percent closure at Day 16 versus synaptophysin percent area positive staining in the hippocampus for the filtered cohort (n=41), with Spearman correlation line shown (rs = 0.047, p = 0.772). C. Representative 20x cerebellum image. D. Scatter plot of wound healing percent closure at Day 16 versus synaptophysin percent area positive staining in the cerebellum (n=38), with Spearman correlation line shown (rs = 0.032, p = 0.849). ns = not significant.

Glial Fibrillary Acidic Protein (GFAP) immunostaining, a marker of astrocyte activation and reactive gliosis, was assessed in hippocampus and cerebellum in the filtered cohort (high n=28, low n=28) (Figure 13). High and low responders showed comparable GFAP expression in both regions. In hippocampus, Spearman's correlation between wound healing and GFAP was non-significant (rs = -0.094, p = 0.493, n = 56), and group comparisons showed no significant difference (high: 4.02 ± 1.67%; low: 4.21 ± 1.67%; t = 0.419, df = 51.66, p = 0.677). Cerebellar GFAP expression was similarly comparable between groups (rs = 0.019, p = 0.893, n = 53; t = 0.188, df = 46.94, p = 0.852). The absence of a significant GFAP difference is notable given that hippocampal transcriptomic analysis identified upward trends in astrocyte-associated genes including Stat3 and Lcn2 in high responders, suggesting that transcriptional upregulation

of astrocyte programs may not be reflected at the level of bulk GFAP protein, or may represent a neuroprotective rather than a reactive astrocyte state (Barres, 2008).

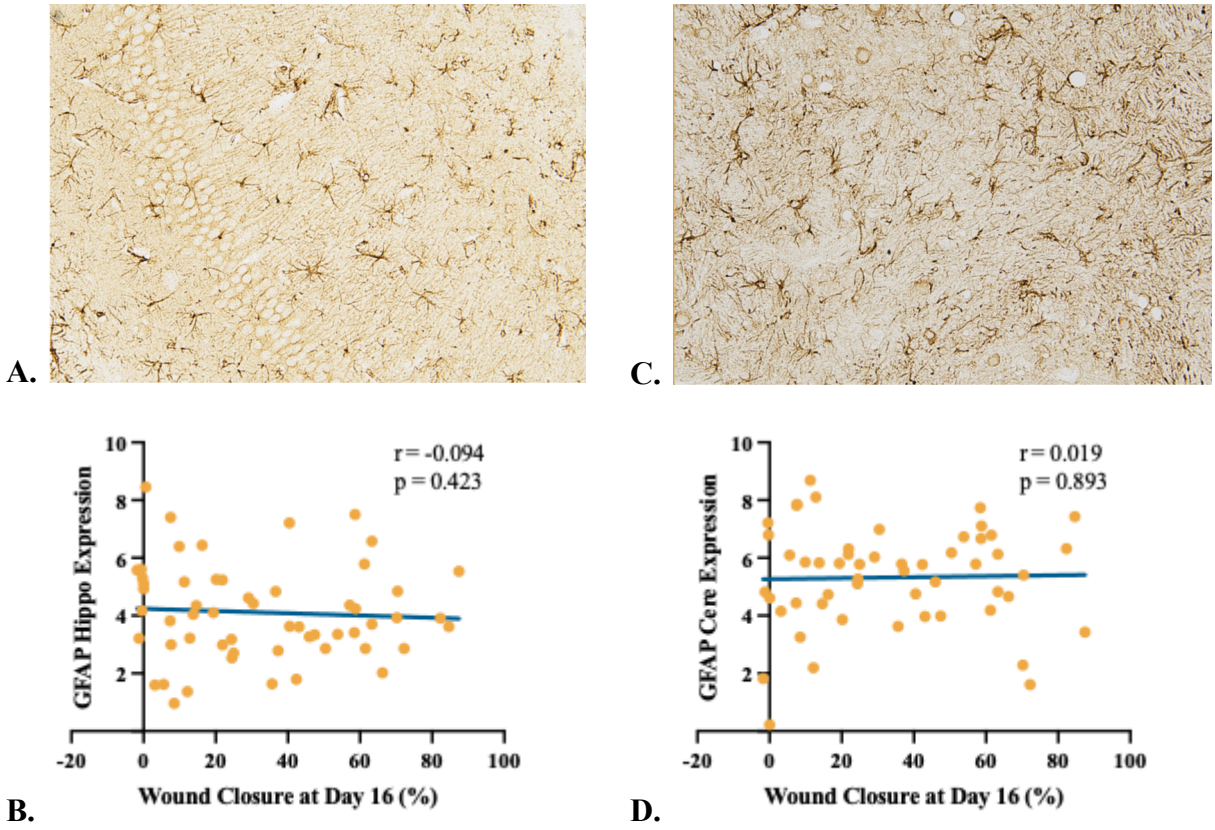

Figure 13. GFAP immunostaining in wound healing responder mice. A. Representative 20x hippocampus image. B. Scatter plot of wound healing percent closure at Day 16 versus GFAP percent area positive staining in the hippocampus for the filtered cohort (n=56), with Spearman correlation line shown (rs = -0.094, p = 0.493). C. Representative 20x cerebellum image. D. Scatter plot of wound healing percent closure at Day 16 versus GFAP percent area positive staining in the cerebellum (n=53), with Spearman correlation line shown (rs = 0.019, p = 0.893). ns = not significant.

Ionized calcium-binding adapter molecule 1 (IBA1) expression, a marker of microglial activation and neuroinflammatory status, was quantified in hippocampus and cerebellum in the filtered cohort (high n=28, low n=28) (Figure 14). Wound healing capacity was significantly negatively correlated with hippocampal IBA1 expression in the full filtered cohort (rs = -0.302, p = 0.024, n = 56), indicating that mice with lower wound healing capacity showed greater microglial marker expression in the hippocampus. Sex-stratified analysis revealed this association was driven primarily by female mice (rs = -0.404, p = 0.024, n = 31), with no significant correlation observed in males (rs = -0.068, p = 0.748, n = 25). Group comparisons between high and low responders did not reach significance for hippocampal IBA1 in the full cohort (high: 2.89 ± 1.89%; low: 3.37 ± 1.89%; t = 0.954, df = 53.30, p = 0.345) or in sex-stratified analyses (females: t = 1.913, df = 25.64, p = 0.067; males: t = 0.282, df = 22.11, p = 0.781). Cerebellar IBA1 expression was comparable between groups in the full cohort (rs = -0.047, p = 0.736, n = 54; t = 0.027, df = 46.60, p = 0.978). Homeostatic microglial markers P2ry12 and Sall1 trended upward in high responders in the hippocampal DESeq2 data,

suggesting that the groups may differ in microglial activation state rather than overall microglial density (Colonna & Butovsky, 2017).

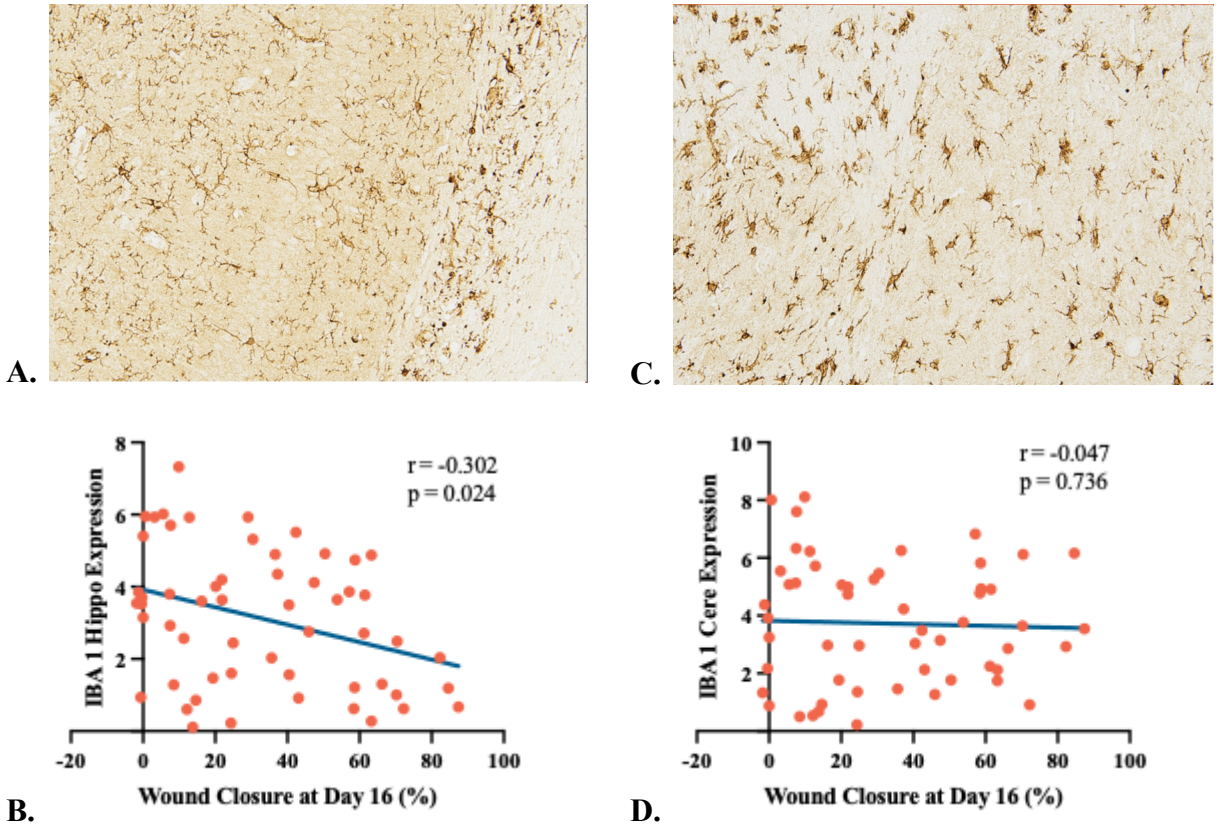

Figure 14. IBA1 immunostaining in wound healing responder mice. A. Representative 20x hippocampus image. B. Scatter plot of wound healing percent closure at Day 16 versus IBA1 percent area positive staining in the hippocampus for the full filtered cohort (n=56), with Spearman correlation line shown (rs = -0.302, p = 0.024). C. Representative 20x cerebellum image. D. Scatter plot of wound healing percent closure at Day 16 versus IBA1 percent area positive staining in the cerebellum (n=54), with Spearman correlation line shown (rs = -0.047, p = 0.736). *p < 0.05 for hippocampus correlation. See Figure 15 for sex-stratified analysis.

Wound healing capacity was significantly negatively correlated with hippocampal IBA1 expression in the full filtered cohort (rs = -0.302, p = 0.024, n = 56) (Figure 15), indicating that mice with lower wound healing capacity showed greater microglial marker expression in the hippocampus. Sex-stratified analysis revealed this association was driven primarily by female mice (rs = -0.404, p = 0.024, n = 31), with no significant correlation observed in males (rs = -0.068, p = 0.748, n = 25). Despite these correlational findings, group comparisons between high and low responders did not reach significance for hippocampal IBA1 in the full cohort (high: 2.89 ± 1.89%; low: 3.37 ± 1.89%; t = 0.954, df = 53.30, p = 0.345) or in sex-stratified analyses (females: t = 1.913, df = 25.64, p = 0.067; males: t = 0.282, df = 22.11, p = 0.781).

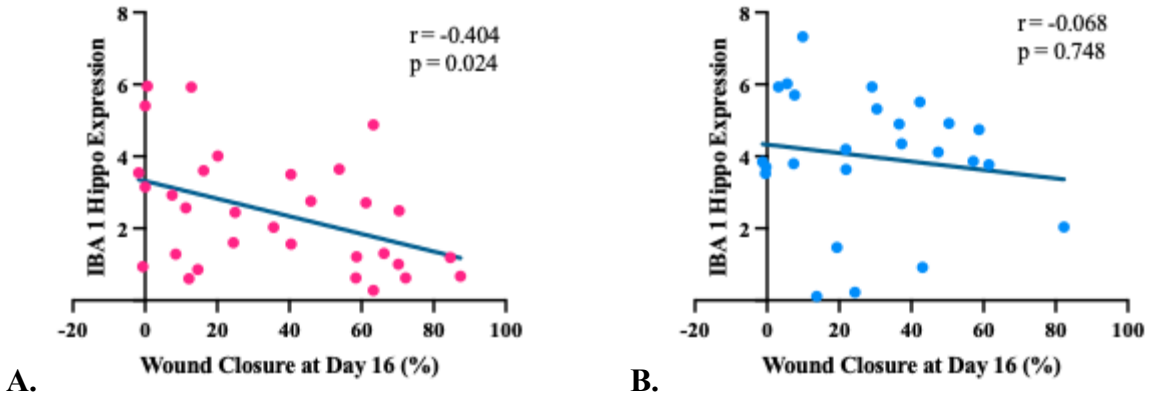

Figure 15. Sex-stratified Spearman correlations between wound healing capacity and hippocampal IBA1 percent area positive staining. A. Female mice (rs = -0.404, p = 0.024, n = 31). B. Male mice (rs = -0.068, p = 0.748, n = 25). Spearman correlation lines shown. *p < 0.05, ns = not significant.

Hematoxylin and eosin staining was performed on brain and peripheral organs to assess general tissue morphology and identify pathological changes between groups. Sections from brain, heart, liver, kidney, and pancreas were evaluated for fibrosis, inflammatory infiltration, and other age-related changes.

Hematoxylin and eosin staining was performed on brain sections from all 66 mice to assess general neuropathology and identify age-related pathological changes between high and low wound healing responder groups. Three histopathological features were scored semiquantitatively (0=absent, 1=mild/present, 2=moderate/severe): thalamic and medullary mineralization, intracytoplasmic inclusion bodies (ICIBs), and axonal spheroids/neuronal axonal dystrophy (NAD). Scores were compared between groups using the Mann-Whitney U test, appropriate for ordinal data.

ICIBs were identified in 94% of mice in both high and low responder groups (30/32 and 32/34, respectively), consistent with the known prevalence of this age-related background finding in aged C57BL/6J mice. Thalamic and medullary mineralization was largely absent, with the majority of mice in both groups scoring 0 (High: 22/32; Low: 22/34), and no significant difference in mineralization scores between groups (High: median=0, mean=0.34±0.55; Low: median=0, mean=0.38±0.55; U=523.0, p=0.749). Axonal spheroids/NAD were present at similar levels in both groups (High: median=1, mean=0.72±0.73; Low: median=1, mean=0.82±0.80; U=508.0, p=0.624). Sporadic age-related findings noted on individual slides included hydrocephalus (n=2), enlarged lateral ventricles (n=3), and a presumptive pituitary neoplasm (n=1); these were not systematically associated with wound healing phenotype.

Hematoxylin and eosin staining was performed on liver, kidney, heart, and pancreas sections from 52 animals with group assignments (high n=28, low n=24) to evaluate peripheral organ pathology between wound healing responder groups. All lesions were scored semiquantitatively using standardized criteria by a board-certified veterinary pathologist (J.M. Snyder, DVM, MS, DACVP), and scores were compared between groups using the Mann-Whitney U test, appropriate for ordinal data.

In the liver, no significant differences were observed between high and low responders across any scoring category, including hepatic degeneration and necrosis (U=360.5, p=0.559), hepatic lipidosis (U=373.0, p=0.459), periportal inflammation (U=342.0, p=0.864), bile duct hyperplasia and cysts (U=323.5, p=0.816), lymphoid aggregates (U=322.0, p=0.789), microgranulomas (U=312.0, p=0.604), Ito cell hyperplasia (U=358.0, p=0.393), telangiectasia (U=322.0, p=0.298), or neoplasia (U=316.0, p=0.545). Background age-related hepatic changes were prevalent across both groups, including hepatic lipidosis (median score 1 in both groups), lymphoid aggregates, and bile duct changes, consistent with normal aging pathology in this strain. Neoplastic lesions identified in the liver included hepatocellular carcinoma (n=2), round cell tumors presumptively identified as lymphoma (n=4), and one presumptive hepatic stellate cell tumor; these were distributed across both groups and did not differ significantly between them.

In the kidney, no significant differences were found between high and low responders in nephropathy (U=255.0, p=0.221), pyelonephritis (U=322.0, p=1.000), infarcts (U=321.0, p=0.990), lymphoid accumulations (U=301.0, p=0.465), mineralization (U=365.5, p=0.145), amyloid (U=322.0, p=1.000), or neoplasia (U=320.0, p=0.481). Nephropathy was the most prevalent finding, present at moderate severity (median score 1 in high responders, 2 in low responders), consistent with the known susceptibility of aged C57BL/6J mice to progressive nephropathy.In the heart, no significant differences were identified between groups in cardiomyopathy (U=285.0, p=0.405), arteriosclerosis (U=357.0, p=0.486), myocardial inflammation (U=328.5, p=0.916), or lymphoid accumulations (U=303.0, p=0.601). Both groups showed prevalent low-grade arteriosclerosis and lymphoid accumulations as background age-related findings.

In the pancreas, no scoring category reached statistical significance, including exocrine atrophy (U=226.0, p=0.084), chronic pancreatitis (U=300.5, p=0.505), fatty infiltration (U=314.5, p=0.848), lymphoid accumulations (U=303.5, p=0.671), islet hyperplasia (U=279.0, p=0.298), or neoplasia (U=294.0, p=0.122). Pancreatic exocrine atrophy showed the most directionally consistent trend, with low responders exhibiting higher median scores (median=1, mean=0.91) compared to high responders (median=0, mean=0.64), though this did not reach the significance threshold (p=0.084). Across all four peripheral organs, no histopathological scoring category reached statistical significance.

Transcriptomic profiling was conducted in hippocampus and liver from male high responders (n=4) and male low responders (n=4) to characterize molecular differences between wound healing phenotypes. Differential expression analysis was performed using PyDESeq2, and pathway-level analysis was performed using preranked GSEA against MSigDB Hallmark gene sets.

No genes reached statistical significance in hippocampus after Benjamini-Hochberg multiple testing correction (Figure 16). Of 21,103 genes analyzed, the minimum adjusted p-value was 0.212. This null result is consistent with the modest effect sizes expected in aging comparisons and with the limited statistical power inherent to the sample size of n=4 per group when correction is applied across a genome-wide scale. Examination of genes ranked by raw p-value revealed several biologically relevant directional trends. Genes associated with glucocorticoid signaling and hypothalamic-pituitary-adrenal axis regulation, specifically Fkbp5 (log2FC = -0.25, p = 0.001) and Klf9 (log2FC = -0.20, p = 0.003), were downregulated in high

responders relative to low responders, suggesting reduced chronic stress hormone signaling in the resilient phenotype. The hypoxia-inducible factor pathway suppressor Hif3a was also downregulated in high responders (log2FC = -0.93, p = 0.001). Conversely, the neuroprotective lectin Lgals1 trended upward in high responders (log2FC = +0.51, p = 0.002). These directional trends did not survive multiple testing correction and should be interpreted as hypothesis-generating rather than confirmatory findings.

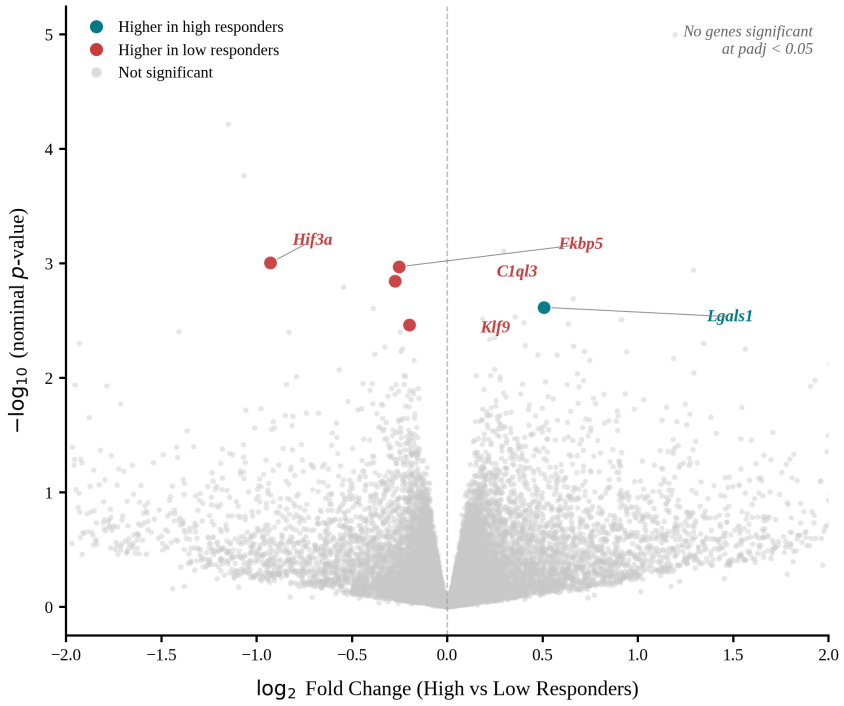

Figure 16. Differential gene expression in hippocampus of high versus low wound healing responder mice. Volcano plot showing -log10(nominal p-value) versus log2 fold change for all 21,103 genes analyzed. Positive values on the x-axis indicate higher expression in high responders. No genes exceeded the Benjamini-Hochberg adjusted significance threshold of padj < 0.05. Key genes with the smallest nominal p-values are labeled. n = 4/group.

The Hallmark Interferon Alpha Response was the only pathway reaching statistical significance in hippocampus, enriched in high responders (NES = 1.71, FDR = 0.016) (Figure 17). This was the sole Hallmark gene set to meet the FDR < 0.05 threshold in the hippocampus analysis. The Hallmark Interferon Gamma Response showed a positive enrichment trend in high responders (NES = 1.52, FDR = 0.111) but did not reach significance. No pathways were significantly enriched in low responders at FDR < 0.25.

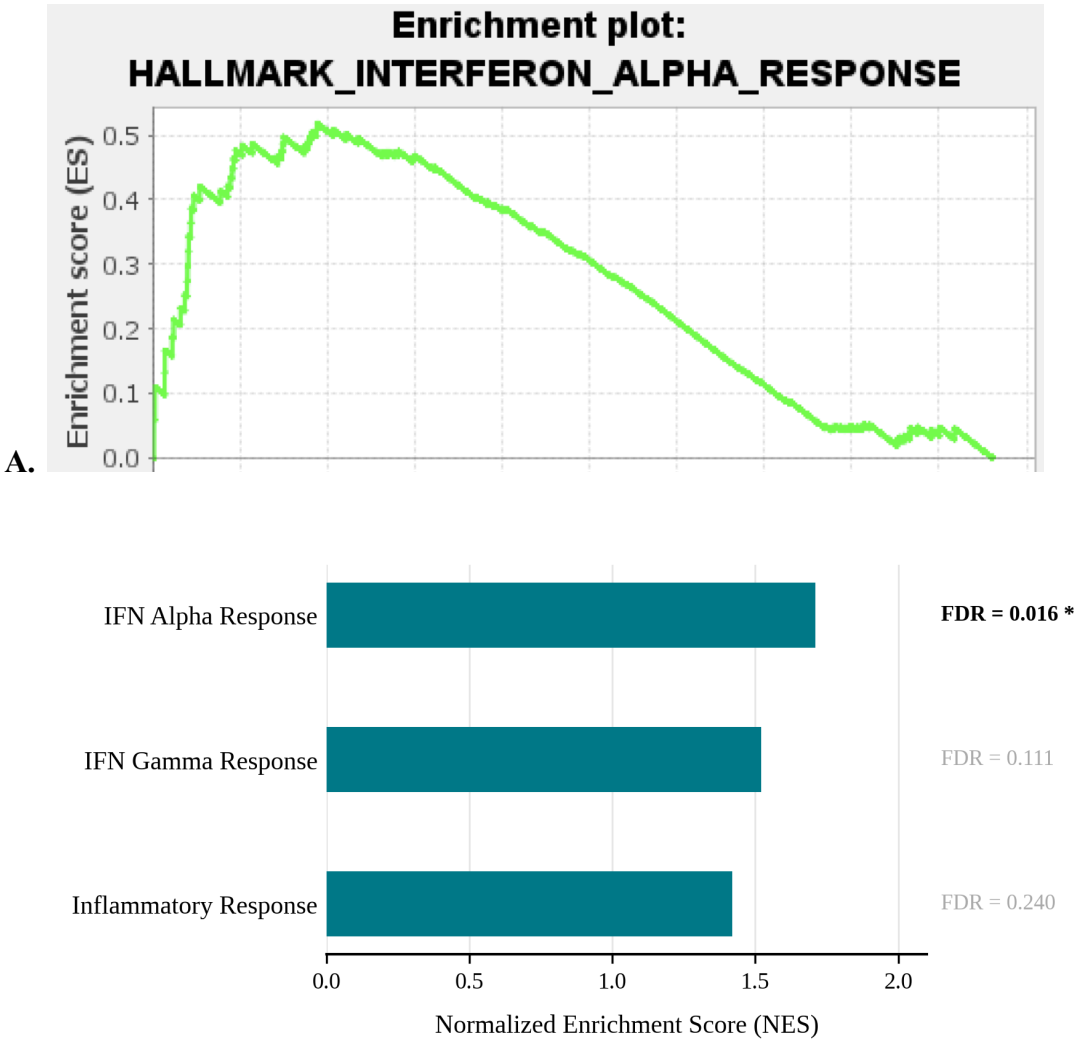

Figure 17. Gene set enrichment analysis of hippocampus transcriptome. A. Enrichment plot for the Hallmark Interferon Alpha Response gene set, the only pathway reaching statistical significance (NES = 1.71, FDR = 0.016), enriched in high responders. B. Summary of all Hallmark pathways with FDR < 0.25, ordered by normalized enrichment score. Positive NES indicates enrichment in high responders. n = 4/group.

Fourteen genes were differentially expressed in liver at padj < 0.05, comprising 6 upregulated and 8 downregulated in high responders (Figure 18, Table 2). Of 18,426 genes analyzed, this set of 14 genes represented the most robust molecular differences between wound healing phenotypes. Among upregulated genes, Gadd45g showed the largest fold change (log2FC = +1.87, padj = 0.004). Gadd45g encodes a stress-responsive protein involved in DNA damage response and cell cycle arrest, and is a transcriptional target of p53. Additional upregulated genes included Slc26a10 (log2FC = +1.60, padj = 0.004), involved in sulfate transport and detoxification; Cyp26a1 (log2FC = +1.32, padj = 0.008), a cytochrome P450 enzyme regulating retinoic acid metabolism; Gstm3 (log2FC = +1.26, padj = 0.022), a glutathione S-transferase involved in oxidative stress defense (Hayes et al., 2005); Ndrg1

(log2FC = +1.19, padj = 0.004), a stress-responsive gene implicated in hypoxia signaling and cell differentiation; and Cyp1a2 (log2FC = +0.65, padj = 0.022), a cytochrome P450 enzyme involved in drug and toxin metabolism.

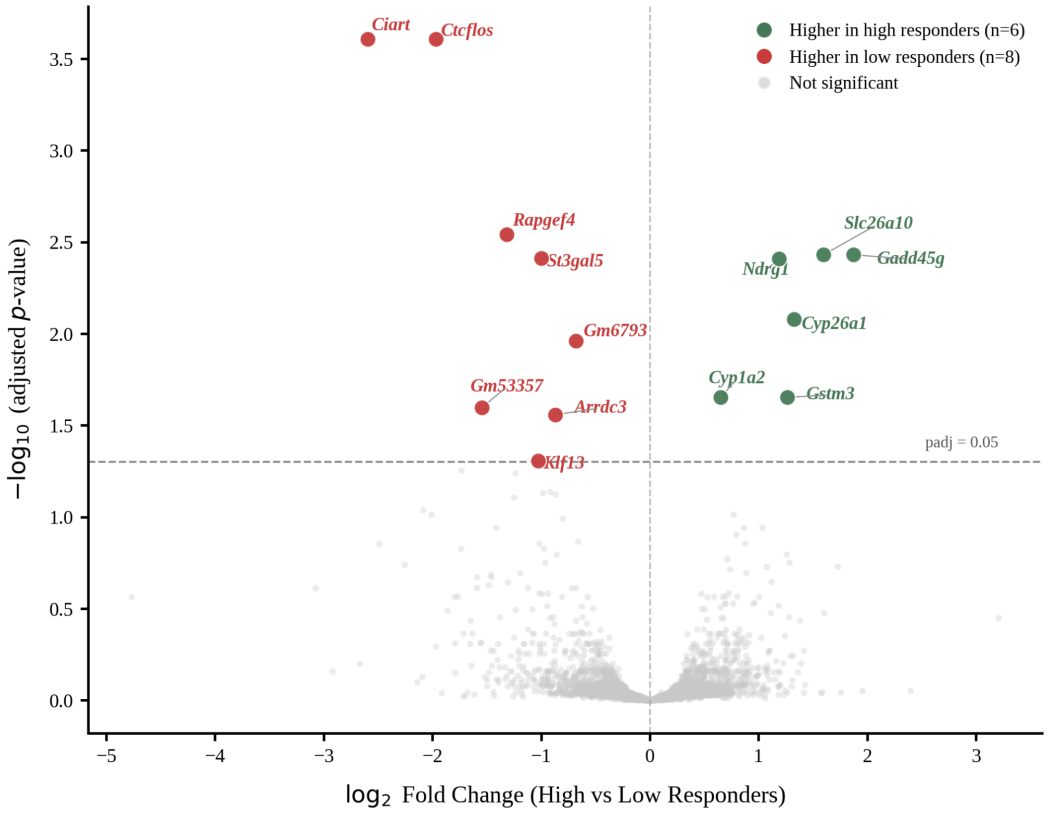

Figure 18. Differential gene expression in liver of high versus low wound healing responder mice. Volcano plot showing -log10(adjusted p-value) versus log2 fold change for all 18,426 genes analyzed. Positive values on the x-axis indicate higher expression in high responders. Significantly differentially expressed genes (padj < 0.05) are highlighted: green = upregulated in high responders (n=6), red = downregulated in high responders (n=8). n = 4/group.

Among genes downregulated in high responders, Ciart showed the largest magnitude of change (log2FC = -2.60, padj = 0.0002) (Table 2). Ciart, also known as CHRONO, encodes a transcriptional repressor of the core circadian clock CLOCK/BMAL1 complex. The strong downregulation of this repressor in high responders suggests reduced suppression of circadian clock activity, and therefore potentially more robust circadian gene expression rhythmicity in the resilient phenotype (Hood & Amir, 2017). The long non-coding RNA Ctcflos was also strongly downregulated (log2FC = -1.97, padj = 0.0002). Additional downregulated genes included Rapgef4 (log2FC = -1.32, padj = 0.003), encoding the cAMP effector Epac2; Klf13 (log2FC = -1.02, padj = 0.049), a Kruppel-like transcription factor involved in inflammatory gene regulation; St3gal5 (log2FC = -1.00, padj = 0.004), a glycolipid biosynthesis enzyme; and Arrdc3 (log2FC = -0.87, padj = 0.028), involved in energy metabolism and adipogenesis regulation.

Table 2. Differentially expressed genes in liver of high versus low wound healing responders (padj < 0.05). Genes are listed by direction of effect. log2FC = log2 fold change in high versus low responders. padj = Benjamini-Hochberg adjusted p-value.

Gene	Base Mean	Log2FC	padj	Direction
Arrdc3	4358.4	-0.870	0.0277	Low > High
Ciart	87.0	-2.597	0.0002	Low > High
Ctcflos	156.9	-1.969	0.0002	Low > High
Cyp1a2	8072.5	0.653	0.0223	High > Low
Cyp26a1	1206.2	1.325	0.0083	High > Low
Gadd45g	97.3	1.871	0.0037	High > Low
Gm53357	63.0	-1.542	0.0253	Low > High
Gm6793	984.5	-0.680	0.0109	Low > High
Gstm3	2408.9	1.263	0.0223	High > Low
Klf13	701.9	-1.024	0.0493	Low > High
Ndrg1	297.5	1.190	0.0039	High > Low
Rapgef4	1819.9	-1.315	0.0029	Low > High
Slc26a10	57.9	1.597	0.0037	High > Low
St3gal5	1213.7	-0.998	0.0039	Low > High

Gene set enrichment analysis of liver revealed distinct pathway signatures in high and low wound healing responders (Figure 19, Table 3). Several pathways trended toward enrichment in high responders, while a larger set reached statistical significance in low responders. Among pathways trending toward enrichment in high responders, Hallmark Cholesterol Homeostasis showed the most prominent enrichment (NES = 1.53, FDR = 0.063), followed by the Hallmark P53 Pathway (NES = 1.30, FDR = 0.153) and Hallmark Oxidative Phosphorylation (NES = 1.29, FDR = 0.140). None of the pathways enriched in high responders reached the FDR < 0.05 significance threshold.

A distinct and statistically significant set of pathways was enriched in low responders. The Hallmark Protein Secretion pathway showed the largest magnitude of enrichment in low responders (NES = -1.79, FDR = 0.012), consistent with increased hepatic secretion of acute phase proteins and inflammatory mediators. Additional significantly enriched pathways in low responders included Hallmark IL6/JAK/STAT3 Signaling (NES = -1.70, FDR = 0.009), Hallmark Complement (NES = -1.67, FDR = 0.010), Hallmark Interferon Gamma Response (NES = -1.60, FDR = 0.017), Hallmark Mitotic Spindle (NES = -1.73, FDR = 0.010), Hallmark MYC Targets V2 (NES = -1.73, FDR = 0.014), and Hallmark E2F Targets (NES = -1.61, FDR =

0.018). The Hallmark Unfolded Protein Response was also significantly enriched in low responders (NES = -1.43, FDR = 0.088), indicating elevated endoplasmic reticulum stress.

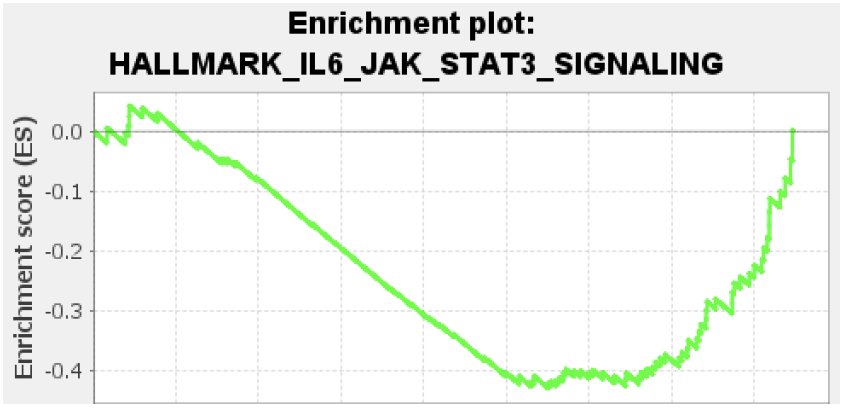

A.

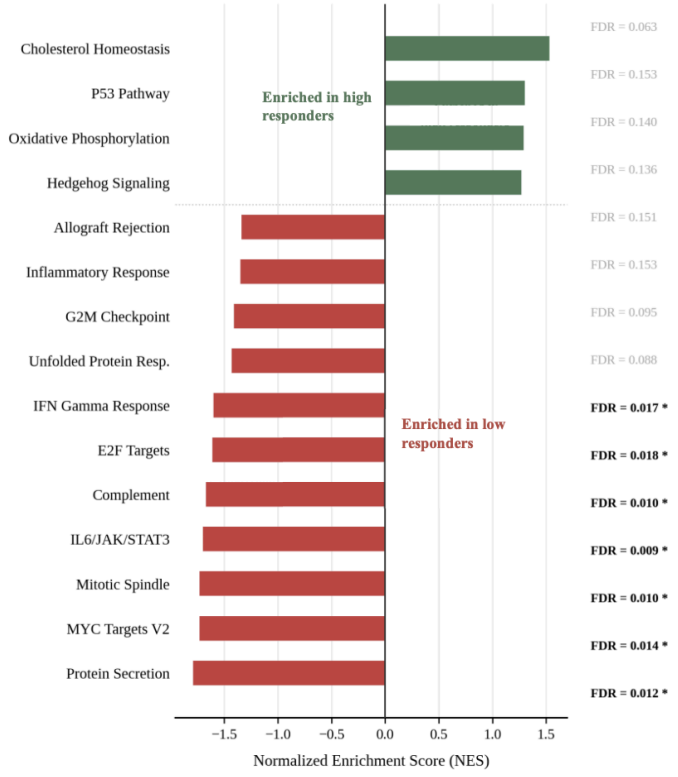

B.

Figure 19. Gene set enrichment analysis of liver transcriptome. A. Enrichment plot for the Hallmark IL6/JAK/STAT3 Signaling pathway, the most significantly enriched pathway in low responders (NES = -1.70, FDR = 0.009). B. Summary of all Hallmark pathways with FDR < 0.25, ordered by normalized enrichment score. Positive NES indicates enrichment in high responders; negative NES indicates enrichment in low responders. Pathways with FDR < 0.05 are marked with an asterisk. n = 4/group.

Table 3. Gene set enrichment analysis results for liver transcriptome. Hallmark pathways with FDR < 0.25 are listed, ordered by normalized enrichment score. Positive NES indicates enrichment in high responders; negative NES indicates enrichment in low responders. NES = normalized enrichment score. FDR = false discovery rate.

Gene Set	Size	NES	NOM p-val	FDR q-val	Enriched In
Protein Secretion	92	−1.79	0.001	0.012	Low
Mitotic Spindle	199	−1.73	< 0.001	0.01	Low
MYC Targets V2	58	−1.73	< 0.001	0.014	Low
IL6/JAK/STAT3 Signaling	79	−1.70	0.003	0.009	Low
Complement	170	−1.67	< 0.001	0.01	Low
E2F Targets	196	−1.61	0.001	0.018	Low
Interferon Gamma Response	182	−1.60	< 0.001	0.017	Low
Unfolded Protein Response	110	−1.43	0.015	0.088	Low
G2M Checkpoint	190	−1.41	0.008	0.095	Low
Inflammatory Response	161	−1.35	0.034	0.153	Low
Allograft Rejection	169	−1.34	0.032	0.151	Low
Myogenesis	152	1.56	< 0.001	0.089	High
Cholesterol Homeostasis	71	1.53	0.016	0.063	High
KRAS Signaling DN	102	1.33	0.064	0.204	High
Estrogen Response Late	167	1.31	0.02	0.18	High
P53 Pathway	190	1.3	0.026	0.153	High
Oxidative Phosphorylation	193	1.29	0.028	0.14	High

Discussion

This study investigated whether wound healing capacity at 18 months of age predicts physiological and cognitive resilience in aged C57BL/6J mice at 24 to 25 months, and whether molecular signatures in hippocampus and liver distinguish high from low responders. Mice stratified by median wound closure demonstrated substantial heterogeneity in healing capacity, ranging from wound enlargement to near-complete closure, consistent with the natural individual variation in physiological response previously documented in this strain (Jiang et al., 2020; Daneshjoo et al., 2022). While wound healing stratification did not produce statistically significant group differences across all behavioral outcome measures in the unfiltered pooled cohort, rotarod performance reached significance in the filtered cohort, and transcriptomic profiling of liver revealed a coherent and biologically meaningful molecular signature distinguishing high from low responders, with low responders showing a convergent pattern of inflammatory activation, cellular stress, and hepatocyte turnover. These findings suggest that wound healing capacity captures biologically meaningful differences in aging phenotypes at the molecular level, even when behavioral differences are not uniformly detectable across all assays and cohort compositions.

Behavioral Outcomes

High and low wound healing responders did not differ significantly on box maze learning index, Y-maze spontaneous alternation, grip strength, or rotarod performance in the full pooled cohort analysis. However, following exclusion of animals exhibiting net wound enlargement (below -10%, n = 10), a more coherent pattern emerged. Rotarod performance reached significance in the full filtered cohort ($t = 2.309$, $df = 50.13$, $p = 0.025$), and sex-stratified analysis revealed a significant association between wound healing capacity and rotarod performance in male mice specifically ($r_s = 0.575$, $p = 0.003$; $t = 2.597$, $df = 21.42$, $p = 0.017$), with high-healing males demonstrating substantially longer latency to fall than low-healing males. No significant sex-specific associations were identified for learning index, Y-maze alternation, or grip strength in either sex. These findings contrast with Jiang and colleagues (2020), in which fast-healing female C57BL/6J mice at 23 months significantly outperformed slow healers on box maze spatial learning, forelimb grip strength, and voluntary wheel running. The present cohort enrolled both sexes at 18 months with behavioral testing at 24 to 25 months, a later timepoint at which floor effects in cognitive and physical performance may have compressed detectable group differences. The emergence of significant rotarod findings following exclusion of negative healers and sex stratification suggests these prior null results reflected both cohort composition and the diluting effect of including biologically distinct animals.

The inclusion of both sexes without sex-stratified primary analysis may have obscured wound healing-dependent differences that are sex-specific. The Ladiges laboratory has previously documented sex-dependent treatment effects in related aging models, in which interventions produced significant outcomes in one sex but not the other (Mazzola, 2025). Male and female C57BL/6J mice differ in wound healing physiology, inflammatory responses, and behavioral performance across multiple assays. The male-specific association between wound healing and motor coordination is biologically plausible, as rotarod performance depends on integrated cerebellar, neuromuscular, and sensory function that deteriorates with age, and whether wound

healing capacity differentially predicts these systems in males versus females warrants further investigation (Shiotsuki et al., 2010).

A subset of animals (n = 10) exhibited net wound enlargement at Day 16 and were excluded from primary analyses on the basis that this pattern likely reflects a qualitatively distinct biological response rather than attenuated healing capacity. Consistent with this interpretation, these animals did not differ significantly from moderate or positive healers on any functional outcome, and their performance on rotarod and Y-maze fell within the range of the other groups rather than below them. Whether extreme wound enlargement in aged mice reflects immune dysregulation, a frailty-adjacent state, or unmeasured environmental variables remains an open question that future studies with immune profiling data would be well-positioned to address.

Hippocampal Transcriptomics

Differential expression analysis of hippocampal tissue identified no genes reaching significance after multiple testing correction at padj < 0.05, a finding consistent with the modest effect sizes expected in aged, genetically homogeneous animals and with the limited statistical power inherent to n=4 per group when correction is applied across more than 21,000 genes. This null result should not be interpreted as an absence of biologically meaningful transcriptomic differences between high and low responders, but rather as a reflection of current sample size constraints. Examination of directional trends in genes ranked by nominal p-value revealed several convergent signals. Fkbp5 and Klf9, both glucocorticoid-regulated genes involved in hypothalamic-pituitary-adrenal axis signaling, trended downward in high responders relative to low responders. Fkbp5 encodes a co-chaperone that modulates glucocorticoid receptor sensitivity and is a well-established molecular marker of chronic stress exposure (Binder, 2009). Lower Fkbp5 expression in high responders suggests reduced chronic glucocorticoid tone in the resilient phenotype, a finding consistent with evidence that chronic stress hormone signaling contributes to hippocampal neuronal loss and cognitive decline in aging (McEwen et al., 2016). Klf9, a transcription factor induced by glucocorticoids and thyroid hormone, also trended downward in high responders, reinforcing the pattern of reduced HPA axis activation in the hippocampus of the resilient group.

Gene set enrichment analysis identified the Hallmark Interferon Alpha Response as the only pathway reaching statistical significance in hippocampus, with enrichment in high responders (NES = 1.71, FDR = 0.016). Type I interferon signaling in the central nervous system has complex and context-dependent effects. At low to moderate levels, interferon alpha supports neuroprotective innate immune surveillance, promotes clearance of cellular debris, and facilitates synaptic maintenance (Blank & Prinz, 2017). This is distinct from the pro-inflammatory interferon gamma signaling enriched in low responders' livers, which is associated with peripheral tissue damage responses and systemic immune activation. The hippocampal interferon alpha enrichment in high responders may therefore reflect a constitutively more active innate immune surveillance program in the resilient aging brain, rather than a pathological neuroinflammatory response. This interpretation is supported by the upward trend in the neuroprotective lectin Lgals1 in high responders (log2FC = +0.51, p = 0.002), as galectin-1 promotes neuronal survival and supports neurogenesis in aging hippocampus (Kajitani et al., 2009). Together, these hippocampal transcriptomic trends suggest that high responders maintain a more neuroprotective molecular environment, characterized by reduced stress hormone

signaling and enhanced innate immune surveillance, though validation in a larger cohort will be necessary to confirm these directional findings.

Hepatic Transcriptomics

The most robust molecular findings in this study emerged from liver transcriptomics, where 14 genes were differentially expressed between high and low responders at padj < 0.05, and gene set enrichment analysis identified multiple statistically significant pathway-level differences. The pattern of findings was strikingly coherent across both levels of analysis and pointed to two distinct biological programs characterizing the high and low responder liver phenotypes.

High responders showed upregulation of genes associated with cellular stress sensing and detoxification, including Gadd45g (log2FC = +1.87), Gstm3 (log2FC = +1.26), Ndrg1 (log2FC = +1.19), Cyp26a1 (log2FC = +1.32), and Cyp1a2 (log2FC = +0.65). Gadd45g is a p53 target gene involved in DNA damage sensing and controlled cell cycle arrest, and its upregulation in high responders is consistent with the trending enrichment of the Hallmark P53 Pathway in high responder livers (NES = 1.30, FDR = 0.153). Gstm3 belongs to the glutathione S-transferase family, enzymes central to phase II detoxification and oxidative stress defense (Hayes et al., 2005). The upregulation of multiple cytochrome P450 enzymes alongside glutathione transferases in high responders points to a broadly enhanced hepatic detoxification capacity, consistent with the trending enrichment of Hallmark Oxidative Phosphorylation (NES = 1.29, FDR = 0.140) and Cholesterol Homeostasis (NES = 1.53, FDR = 0.063) pathways. Together, these data suggest that high responder livers are characterized by more efficient energy metabolism, tighter lipid regulation, and stronger antioxidant defense, reflecting a constitutively more resilient hepatic cellular environment.

The most strongly downregulated gene in high responders was Ciart (log2FC = -2.60, padj = 0.0002), encoding CHRONO, a transcriptional repressor of the core circadian clock CLOCK/BMAL1 complex. CHRONO was simultaneously characterized by two independent research groups as a genuine core clock component: it binds to the C-terminal transactivation domain of BMAL1 and represses CLOCK/BMAL1-driven transcription through an epigenetic mechanism involving histone deacetylase recruitment, with its occupancy at clock gene regulatory regions oscillating in a circadian manner (Goriki et al., 2014; Anafi et al., 2014). Its expression is robustly rhythmic in mouse liver, pituitary, skeletal muscle, and white adipose tissue, and Chrono knockout mice display a measurable lengthening of circadian period, establishing it as a functional clock component rather than a downstream output gene (Goriki et al., 2014; Anafi et al., 2014). The strong and highly significant downregulation of Ciart in high responders at nearly 6-fold linear change (padj = 0.0002) indicates that CLOCK/BMAL1 transcriptional activity faces less repression in the resilient liver, and therefore that circadian-driven gene expression programs may be more robustly sustained in high responders. This is particularly meaningful in the context of aging: Sato and colleagues demonstrated that aging reprograms the hepatic circadian transcriptome in a highly tissue-specific manner, dampening clock-driven metabolic gene expression and disrupting NAD+/SIRT1-regulated acetylation rhythms, while caloric restriction partially rescues these rhythms and extends lifespan (Sato et al., 2017). Circadian clock robustness in the liver is now recognized as a key regulator of hepatic glucose and lipid homeostasis, inflammatory signaling, oxidative stress defense, and mitochondrial function, with clock disruption contributing to metabolic dysfunction in a manner

that worsens with age (Hood & Amir, 2017; Xu & Li, 2023). The Ciart finding therefore positions circadian clock integrity as a candidate molecular mechanism underlying hepatic resilience in high wound healing responders, and suggests that interventions targeting circadian clock robustness, including time-restricted feeding, NAD+ precursor supplementation, or direct modulation of CLOCK/BMAL1 activity, may be particularly relevant therapeutic strategies in the context of wound healing-stratified aging phenotypes. The concurrent downregulation of Rapgef4 (Epac2, log2FC = -1.32) and Arrdc3 (log2FC = -0.87) in high responders further suggests differences in cAMP-regulated metabolic signaling and energy homeostasis between the two groups.

Low responders, by contrast, exhibited a coordinated pattern of pathway enrichment that closely resembles the molecular phenotype of systemic inflammaging. Significant enrichment was observed for IL6/JAK/STAT3 Signaling (NES = -1.70, FDR = 0.009), the Complement cascade (NES = -1.67, FDR = 0.010), Interferon Gamma Response (NES = -1.60, FDR = 0.017), and Protein Secretion (NES = -1.79, FDR = 0.012). The enrichment of IL6/JAK/STAT3 signaling reflects the liver's role as the primary source of acute phase proteins and a key responder to systemic IL-6 signaling, which is chronically elevated in aged organisms with poor functional trajectories (Franceschi et al., 2000; Ferrucci & Fabbri, 2018). Complement activation in low responders indicates ongoing detection of tissue damage signals and systemic immune stress, while the enrichment of protein secretion pathways is consistent with increased hepatic production of inflammatory mediators and acute phase reactants in this group. The concurrent enrichment of cell cycle and DNA damage response pathways including MYC Targets V2 (NES = -1.73, FDR = 0.014), E2F Targets (NES = -1.61, FDR = 0.018), Mitotic Spindle (NES = -1.73, FDR = 0.010), and G2M Checkpoint (NES = -1.41, FDR = 0.095) indicates elevated hepatocyte proliferation in low responders, consistent with compensatory cellular turnover driven by accumulated cellular damage. The Unfolded Protein Response was also significantly enriched in low responders (NES = -1.43, FDR = 0.088), indicating elevated endoplasmic reticulum stress and impaired proteostasis. This convergent multi-pathway signature in low responders is consistent with the hallmarks of aging framework, specifically the interconnected deterioration of intercellular communication, chronic inflammation, and loss of proteostasis that characterizes vulnerable aging phenotypes (López-Otín et al., 2023).

Notably, interferon gamma response was enriched in low responder livers while interferon alpha response was enriched in high responder hippocampus, revealing an important tissue-specific pattern in immune signaling between the two groups. Interferon gamma is primarily a pro-inflammatory type II interferon produced by activated T cells and natural killer cells in response to infection or tissue damage, and its chronic hepatic upregulation in low responders is consistent with a systemic inflammatory environment. Interferon alpha, by contrast, is a type I interferon with primarily antiviral and neuroprotective functions at moderate levels. This reciprocal tissue-specific interferon pattern warrants further investigation.

Immunohistochemical Analysis

Immunohistochemical analysis of brain tissue revealed no statistically significant group differences between high and low wound healing responders across synaptophysin, GFAP, or IBA1 in hippocampus or cerebellum by unpaired t-test. However, Spearman’s correlation analysis identified a significant negative relationship between wound healing capacity and

hippocampal IBA1 expression in the full filtered cohort (rs = -0.302, p = 0.024, n = 56), indicating that mice with lower wound healing capacity showed greater microglial marker expression in the hippocampus across the continuous range of healing values. Sex-stratified analysis revealed this association was driven primarily by female mice (rs = -0.404, p = 0.024, n = 31), with no significant correlation observed in males (rs = -0.068, p = 0.748, n = 25). The female-specific nature of this finding is consistent with documented sex differences in microglial activation states and neuroinflammatory responses to aging in C57BL/6J mice, in which female microglia exhibit greater transcriptional reactivity and higher baseline expression of inflammatory markers compared to males (Guneykaya et al., 2018). The hippocampal IBA1 correlation is directionally consistent with the hepatic inflammaging signature identified by RNA sequencing, in which low responders showed significant enrichment of IL6/JAK/STAT3 signaling, complement activation, and interferon gamma response pathways, suggesting that poor wound healing capacity co-occurs with a broader pattern of systemic inflammatory dysregulation that manifests both peripherally and centrally. The absence of a significant GFAP protein difference despite transcriptomic upregulation of astrocyte-associated genes in high responders is consistent with prior evidence that type I interferon-driven astrocyte programs do not necessarily manifest as increased GFAP immunoreactivity (Barres, 2008). Synaptophysin and BDNF expression were both comparable between groups in hippocampus and cerebellum, with no significant correlations or group differences detected in either sex. The absence of a BDNF difference at the protein level is consistent with the lack of significant differential expression for Bdnf transcript in hippocampal RNA sequencing, and does not preclude the possibility that BDNF signaling differs at the receptor, post-translational, or synaptic release level in ways not captured by bulk immunohistochemistry. Neuropathological assessment of brain H&E sections revealed no significant differences between groups in mineralization (U=523.0, p=0.749) or spheroids/NAD (U=508.0, p=0.624), with ICIBs present as a ubiquitous age-related background finding in both groups (94% prevalence). Histopathological evaluation of peripheral organs across liver, kidney, heart, and pancreas revealed no statistically significant differences between high and low responders in any scoring category. Pancreatic exocrine atrophy showed the most directionally consistent trend, with low responders exhibiting higher scores than high responders (median 1 vs. 0; U=226.0, p=0.084), which is consistent with the broader hepatic metabolic signature identified by RNA sequencing and warrants follow-up in larger cohorts. Age-related background changes including hepatic lipidosis, lymphoid aggregates, nephropathy, and low-grade arteriosclerosis were prevalent across both groups, reflecting the expected pathological burden in 24 to 25 month C57BL/6J mice.

Limitations

Several limitations should be considered when interpreting the findings of this study. First, the sample size available for RNA sequencing analysis (n=4 per group) provided limited statistical power for detecting differentially expressed genes after multiple testing correction, particularly in the hippocampus where effect sizes were small and variable. The null DEG result in hippocampus should therefore be interpreted as underpowered rather than as evidence of transcriptomic equivalence between the groups. Larger RNA-seq cohorts will be necessary to characterize hippocampal molecular differences with adequate statistical confidence.

Second, RNA sequencing was conducted exclusively in male mice, while the behavioral cohort included both males and females. This limits the generalizability of transcriptomic findings to the

full cohort and precludes sex-stratified analysis of molecular signatures. Given the documented sex differences in wound healing physiology, immune function, and aging trajectories in C57BL/6J mice, future studies should include sex as a biological variable in both behavioral and transcriptomic analyses.

Third, the median-split stratification approach assigns mice near the threshold to opposing groups based on minimal differences in wound closure percentage. Alternative approaches, including tertile-based stratification excluding middle-group animals or continuous regression-based analyses, may better capture the full relationship between healing capacity and downstream outcomes in larger cohorts. The continuous Spearman correlation approach is better suited to detecting wound healing-dependent relationships across the full range of healing capacity, and the significant rotarod findings in both the full filtered cohort ($p = 0.025$) and in male sex-stratified analysis ($p = 0.017$) support this. Additionally, the relatively late testing timepoint of 24 to 25 months may have reduced behavioral sensitivity. Earlier assessment at 22 to 23 months, as employed by Jiang and colleagues (2020), may provide greater dynamic range for detecting wound healing-dependent differences before more advanced age-related decline compresses performance across individuals.

Finally, this study was conducted in a single inbred mouse strain under controlled laboratory conditions, which may not fully recapitulate the complexity of human aging heterogeneity. Translational validation in outbred animal models or human populations will be necessary before wound healing-based stratification approaches can be applied in clinical contexts.

Future Directions

The findings of this study suggest several productive avenues for future investigation. Sex-stratified analysis of both behavioral and transcriptomic data represents the most immediate priority, as the male-specific wound healing-motor coordination relationship and the female-specific wound healing-hippocampal IBA1 correlation suggest that wound healing capacity may predict distinct downstream aging outcomes depending on sex. Replication of these sex-specific findings in a larger, sex-balanced cohort with adequate power within each sex is necessary before firm conclusions can be drawn. Larger RNA sequencing cohorts, ideally with n=8 to 10 per group, would provide the statistical power necessary to characterize hippocampal differential expression with confidence and to conduct sex-stratified transcriptomic analyses. The female-specific IBA1 correlation provides a specific hypothesis for future hippocampal transcriptomic work: whether microglial activation state differs between high and low wound healing responders in females in a manner consistent with the broader inflammaging signature observed in low responder livers. The hepatic inflammaging signature identified in low responders provides a strong foundation for testing targeted interventions, including senolytics, anti-inflammatory agents, and circadian-modulating compounds, in wound healing-stratified cohorts. The strong downregulation of Ciart in high responders is a particularly tractable target, given the growing availability of pharmacological tools for modulating circadian clock components and the established links between hepatic circadian robustness and healthy aging (Goriki et al., 2014; Anafi et al., 2014; Hood & Amir, 2017; Sato et al., 2017). Finally, the potential of wound healing as a biomarker warrants validation in human cohorts, where minimally invasive wound healing measurements could be integrated into longitudinal aging studies to assess their predictive value for functional outcomes across multiple health domains.

Summary and Conclusion

This study investigated wound healing capacity as an early, non-invasive biomarker of aging resilience in C57BL/6J mice, pursuing two specific objectives: first, to determine whether wound healing response at 18 months predicts physiological and cognitive function at 24 to 25 months; and second, to characterize the transcriptomic and molecular correlates of wound healing phenotypes across hippocampus and liver. A 2mm ear punch biopsy reliably stratified aged mice into high and low responders based on wound closure at Day 16, confirming that individual variation in healing capacity is readily quantifiable in this model. Body weight was comparable between groups throughout the study, establishing that stratification reflected wound healing physiology rather than general health status.

Comprehensive behavioral phenotyping across four assays assessing spatial learning, working memory, motor coordination, and grip strength revealed significant associations between wound healing capacity and functional outcomes following exclusion of 10 animals exhibiting net wound enlargement and application of sex-stratified analyses. In the filtered cohort (n=56), high healers significantly outperformed low healers on rotarod performance ($t = 2.309$, $df = 50.13$, $p = 0.025$). Sex-stratified analyses identified wound healing capacity as significantly correlated with rotarod performance in male mice specifically ($r_s = 0.575$, $p = 0.003$), with high-healing males demonstrating substantially longer latency to fall than low-healing males ($t = 2.597$, $df = 21.42$, $p = 0.017$). No significant sex-specific associations were identified for learning index, Y-maze alternation, or grip strength in either sex. These findings are interpreted in light of several study design considerations, including the mixed-sex composition of the cohort, the later behavioral testing timepoint relative to prior work from this laboratory, and the use of a median-split stratification approach in a dataset with high individual variability. The emergence of a significant rotarod result in the full filtered cohort, and the robust male-specific correlation, demonstrate that wound healing-dependent differences in motor resilience are detectable within this expanded longitudinal design.

Spearman's correlation analysis of immunohistochemical outcomes identified a significant negative relationship between wound healing capacity and hippocampal IBA1 expression in the full filtered cohort ($r_s = -0.302$, $p = 0.024$, $n = 56$), with sex-stratified analysis revealing this association was driven by female mice ($r_s = -0.404$, $p = 0.024$, $n = 31$). This female-specific finding suggests that poor wound healing capacity co-occurs with greater hippocampal microglial burden in females, consistent with known sex differences in microglial activation states during aging (Guneykaya et al., 2018). No significant group differences or continuous correlations were identified for synaptophysin, GFAP, BDNF, or cerebellar IBA1 in either sex.

Transcriptomic profiling identified a coherent molecular signature distinguishing high and low responders in liver, the most biologically informative finding of this study. Fourteen genes were differentially expressed in liver at $padj < 0.05$, with high responders showing upregulation of genes involved in DNA damage sensing, antioxidant defense, and detoxification, including Gadd45g, Gstm3, Ndrg1, and Cyp26a1. The most strongly downregulated gene in high responders, Ciart, encodes CHRONO, a core repressor of the circadian clock CLOCK/BMAL1 complex (Goriki et al., 2014; Anafi et al., 2014), suggesting that resilient animals maintain more robust circadian gene expression rhythmicity and less suppression of clock-driven hepatic metabolic programs (Hood & Amir, 2017; Sato et al., 2017). Gene set enrichment analysis

reinforced these gene-level findings: high responder livers trended toward enrichment of oxidative phosphorylation, cholesterol homeostasis, and p53 pathway activity, while low responder livers were significantly enriched for the hallmarks of inflammaging, including IL6/JAK/STAT3 signaling, complement activation, interferon gamma response, elevated protein secretion, endoplasmic reticulum stress, and cell cycle and DNA damage response programs indicative of increased hepatocyte turnover. This molecular portrait of the low responder liver is consistent with the broader hallmarks of aging framework and represents a biologically plausible mechanism through which poor wound healing capacity and systemic vulnerability co-occur in aged animals (López-Otín et al., 2023).

Hippocampal transcriptomics yielded no differentially expressed genes after multiple testing correction, a result attributable to limited statistical power at n=4 per group across more than 21,000 tested genes. Directional trends in nominal p-value rankings nonetheless identified biologically coherent signals, with glucocorticoid stress axis genes Fkbp5 and Klf9 trending downward in high responders, suggesting reduced chronic hypothalamic-pituitary-adrenal axis activation in the resilient phenotype. Gene set enrichment analysis identified the Interferon Alpha Response pathway as significantly enriched in high responder hippocampus (NES = 1.71, FDR = 0.016), consistent with a neuroprotective innate immune surveillance program in the resilient aging brain. BDNF immunohistochemical quantification in hippocampus showed no significant differences between high and low responders at the protein level ($r_s = -0.046$, $p = 0.739$; $U = 398.0$, $p = 0.928$), consistent with the absence of Bdnf differential expression in hippocampal RNA sequencing.

Collectively, these findings advance the validation of wound healing capacity as a biomarker of aging resilience by demonstrating that high and low wound healing responders are distinguishable at the molecular level in liver, with low responders exhibiting a coordinated pattern of inflammatory, metabolic, and cellular stress signatures that characterize less resilient aging phenotypes. The translational potential of this approach is significant: wound healing assessment is minimally invasive, straightforward to standardize, and assessable early in the aging process when intervention may be most effective. The molecular pathways identified here, particularly circadian clock regulation, hepatic inflammatory signaling, and p53-mediated stress response, represent candidate therapeutic targets for future interventions aimed at promoting resilient aging. Continued work expanding sample sizes, incorporating sex-stratified analyses, and validating findings across additional tissues and mouse strains will be necessary to fully establish the predictive validity of wound healing as a biomarker and to translate these molecular insights toward the development of personalized strategies for healthy longevity.

References

Anafi RC, Lee Y, Sato TK, et al. Machine learning helps identify CHRONO as a circadian clock component. PLoS Biol. 2014;12(4):e1001840. doi:10.1371/journal.pbio.1001840.

Ashcroft GS, Horan MA, Ferguson MW. The effects of aging on cutaneous wound healing in mammals. J Anat. 1995;187(Pt 1):1-26. PMID: 7591980.

Barres BA. The mystery and magic of glia: a perspective on their roles in health and disease. Neuron. 2008;60(3):430-440. doi:10.1016/j.neuron.2008.10.013.

Beard JR, Officer A, de Carvalho IA, et al. The World report on ageing and health: a policy framework for healthy ageing. Lancet. 2016;387(10033):2145-2154. doi:10.1016/S0140-6736(15)00516-4.

Bekinschtein P, Cammarota M, Katche C, et al. BDNF is essential to promote persistence of long-term memory storage. Proc Natl Acad Sci USA. 2008;105(7):2711-2716. doi:10.1073/pnas.0711863105.

Bettio LEB, Rajendran L, Gil-Mohapel J. The effects of aging in the hippocampus and cognitive decline. Neurosci Biobehav Rev. 2017;79:66-86. doi:10.1016/j.neubiorev.2017.04.030.

Binder EB. The role of FKBP5, a co-chaperone of the glucocorticoid receptor in the pathogenesis and therapy of affective and anxiety disorders. Psychoneuroendocrinology. 2009;34(Suppl 1):S186-S195. doi:10.1016/j.psyneuen.2009.05.021.

Blank T, Prinz M. Type I interferon pathway in CNS homeostasis and neurological disorders. Glia. 2017;65(9):1397-1406. doi:10.1002/glia.23154.

Broughton G 2nd, Janis JE, Attinger CE. The basic science of wound healing. Plast Reconstr Surg. 2006;117(7 Suppl):12S-34S. doi:10.1097/01.prs.0000225430.42531.c2.

Colonna M, Butovsky O. Microglia function in the central nervous system during health and neurodegeneration. Annu Rev Immunol. 2017;35:441-468. doi:10.1146/annurev-immunol-051116-052358.

Daneshjoo S, Park JY, Moreno J, Rosenfeld M, Darvas M, Ladiges W. A mouse model of naturally occurring age-related cognitive impairment. Aging Pathobiol Ther. 2022;4(3):87-89. doi:10.31491/apt.2022.09.090.

Darvas M, Mukherjee K, Lee A, Ladiges W. A novel one-day learning procedure for mice. Curr Protoc Mouse Biol. 2020;10(1):e68. doi:10.1002/cpmo.68.

Ferrucci L, Fabbri E. Inflammageing: chronic inflammation in ageing, cardiovascular disease, and frailty. Nat Rev Cardiol. 2018;15(9):505-522. doi:10.1038/s41569-018-0064-2.

Ferrucci L, Gonzalez-Freire M, Fabbri E, et al. Measuring biological aging in humans: a quest. Aging Cell. 2020;19(3):e13080. doi:10.1111/acel.13080.

Flurkey K, Currer JM, Harrison DE. Mouse models in aging research. In: Fox JG, Barthold SW, Davisson MT, et al., eds. The Mouse in Biomedical Research. 2nd ed. Burlington, MA: Academic Press; 2007:637-672.

Franceschi C, Bonafe M, Valensin S, et al. Inflamm-aging: an evolutionary perspective on immunosenescence. Ann N Y Acad Sci. 2000;908:244-254. doi:10.1111/j.1749-6632.2000.tb06651.x.

Gould L, Abadir P, Brem H, et al. Chronic wound repair and healing in older adults: current status and future research. Wound Repair Regen. 2015;23(1):1-13. doi:10.1111/wrr.12245.

Goriki A, Hatanaka F, Myung J, et al. A novel protein, CHRONO, functions as a core component of the mammalian circadian clock. PLoS Biol. 2014;12(4):e1001839. doi:10.1371/journal.pbio.1001839.

Guneykaya D, Ivanov A, Hernandez DP, et al. Transcriptional and translational differences of microglia from male and female brains. Cell Rep. 2018;24(10):2773-2783.e6. doi:10.1016/j.celrep.2018.08.001.

Guo S, DiPietro LA. Factors affecting wound healing. J Dent Res. 2010;89(3):219-229. doi:10.1177/0022034509359125.

Harada CN, Natelson Love MC, Triebel KL. Normal cognitive aging. Clin Geriatr Med. 2013;29(4):737-752. doi:10.1016/j.cger.2013.07.002.

Hayes JD, Flanagan JU, Jowsey IR. Glutathione transferases. Annu Rev Pharmacol Toxicol. 2005;45:51-88. doi:10.1146/annurev.pharmtox.45.120403.095857.

Hood S, Amir S. The aging clock: circadian rhythms and later life. J Clin Invest. 2017;127(2):437-446. doi:10.1172/JCI90328.

Jiang Z, Chen J, Wang J, Mangalindan R, Zhu L, Ladiges WC. A model for studying cutaneous wound healing and resilience to aging: ear punch biopsy in old mice. Aging Pathobiol Ther. 2020;2(3):173-175. doi:10.31491/apt.2020.09.036.

Kajitani K, Nomaru H, Ifuku M, et al. Galectin-1 promotes basal and kainate-induced proliferation of neural progenitors in the dentate gyrus of adult mouse hippocampus. Cell Death Differ. 2009;16(3):417-427. doi:10.1038/cdd.2008.162.

Kennedy BK, Berger SL, Bhatt A, et al. Geroscience: linking aging to chronic disease. Cell. 2014;159(4):709-713. doi:10.1016/j.cell.2014.10.039.

Khalid KA, Nawi AFM, Zulkifli N, Barkat MA, Hadi H. Aging and wound healing of the skin: a review of clinical and pathophysiological hallmarks. Life (Basel). 2022;12(12):2142. doi:10.3390/life12122142.

Kraeuter AK, Guest PC, Sarnyai Z. The Y-maze for assessment of spatial working and reference memory in mice. Methods Mol Biol. 2019;1916:105-111. doi:10.1007/978-1-4939-8994-2_10.

López-Otín C, Blasco MA, Partridge L, Serrano M, Kroemer G. The hallmarks of aging. Cell. 2013;153(6):1194-1217. doi:10.1016/j.cell.2013.05.039.

López-Otín C, Blasco MA, Partridge L, Serrano M, Kroemer G. Hallmarks of aging: an expanding universe. Cell. 2023;186(2):243-278. doi:10.1016/j.cell.2022.11.001.

Mazzola JM. Short-term treatment of mice with GHK peptide enhances resilience to age-related cognitive decline. Master's Thesis. University of Washington; 2025.

McEwen BS, Nasca C, Gray JD. Stress effects on neuronal structure: hippocampus, amygdala, and prefrontal cortex. Neuropsychopharmacology. 2016;41(1):3-23. doi:10.1038/npp.2015.171.

Mootha VK, Lindgren CM, Eriksson KF, et al. PGC-1alpha-responsive genes involved in oxidative phosphorylation are coordinately downregulated in human diabetes. Nat Genet. 2003;34(3):267-273. doi:10.1038/ng1180.

Murman DL. The impact of age on cognition. Semin Hear. 2015;36(3):111-121. doi:10.1055/s-0035-1555115.

Muzellec B, Telénczuk M, Cabeli V, Andreux M. PyDESeq2: a python package for bulk RNA-seq differential expression analysis. Bioinformatics. 2023;39(9):btad547. doi:10.1093/bioinformatics/btad547.

Pais R, Ruano L, Carvalho OP, Barros H. Global cognitive impairment prevalence and incidence in community dwelling older adults: a systematic review. Geriatrics. 2020;5(4):84. doi:10.3390/geriatrics5040084.

Petersen RC, Lopez O, Armstrong MJ, et al. Practice guideline update summary: mild cognitive impairment. Neurology. 2018;90(3):126-135. doi:10.1212/WNL.0000000000004826.

Roenneberg T, Merrow M. The circadian clock and human health. Curr Biol. 2016;26(10):R432-R443. doi:10.1016/j.cub.2016.04.011.

Sato S, Solanas G, Peixoto FO, et al. Circadian reprogramming in the liver identifies metabolic pathways of aging. Cell. 2017;170(4):664-677.e11. doi:10.1016/j.cell.2017.07.042.

Sen CK, Gordillo GM, Roy S, et al. Human skin wounds: a major and snowballing threat to public health and the economy. Wound Repair Regen. 2009;17(6):763-771. doi:10.1111/j.1524-475X.2009.00543.x.

Sgonc R, Gruber J. Age-related aspects of cutaneous wound healing: a mini-review. Gerontology. 2013;59(2):159-164. doi:10.1159/000342344.

Shiotsuki H, Yoshimi K, Shimo Y, et al. A rotarod test for evaluation of motor skill learning. J Neurosci Methods. 2010;189(2):180-185. doi:10.1016/j.jneumeth.2010.03.026.

Singh U, Li J, Seetharam A, Wurtele ES. pyrpipe: a Python package for RNA-Seq workflows. NAR Genomics Bioinformatics. 2021;3(2):lqab049. doi:10.1093/nargab/lqab049.

Smith TD, Adams MM, Gallagher M, Morrison JH, Rapp PR. Circuit-specific alterations in hippocampal synaptophysin immunoreactivity predict spatial learning impairment in aged rats. J Neurosci. 2000;20(17):6587-6593. doi:10.1523/JNEUROSCI.20-17-06587.2000.

Subramanian A, Tamayo P, Mootha VK, et al. Gene set enrichment analysis: a knowledge-based approach for interpreting genome-wide expression profiles. Proc Natl Acad Sci USA. 2005;102(43):15545-15550. doi:10.1073/pnas.0506580102.

United Nations, Department of Economic and Social Affairs, Population Division. World Population Prospects 2019: Highlights (ST/ESA/SER.A/423). New York: United Nations; 2019.

Whitson HE, Duan-Porter W, Schmader KE, Morey MC, Cohen HJ, Colon-Emeric C. Physical resilience in older adults: systematic review and development of an emerging construct. J Gerontol A Biol Sci Med Sci. 2016;71(4):489-495. doi:10.1093/gerona/glv202.

Xu W, Li X. Aging disrupts circadian rhythms in mouse liver mitochondria. Molecules. 2023;28(11):4432. doi:10.3390/molecules28114432.

Yanai S, Endo S. Functional aging in male C57BL/6J mice across the life-span: a systematic behavioral analysis of motor, emotional, and memory function to define an aging phenotype. Front Aging Neurosci. 2021;13:697621. doi:10.3389/fnagi.2021.697621.